

Article

A New Technique for Impervious Surface Mapping and Its Spatio-Temporal Changes from Landsat and Sentinel-2 Images

Lizhong Hua¹, Haibo Wang¹, Huafeng Zhang², Fengqin Sun¹, Lanhui Li¹  and Lina Tang^{3,*} ¹ College of Computer and Information Engineering, Xiamen University of Technology, Xiamen 361024, China² Xiamen Greening Management Center, Xiamen 361004, China³ Key Lab of Urban Environment and Health, Institute of Urban Environment, Chinese Academy of Sciences, Xiamen 361021, China

* Correspondence: lntang@iue.ac.cn; Tel.: +86-592-619-0681

Abstract: Accurately mapping and monitoring the urban impervious surface area (ISA) is crucial for understanding the impact of urbanization on heat islands and sustainable development. However, less is known about ISA spectra heterogeneity and their similarity to bare land, wetland, and high-rise-building shadows. This study proposes a feature-based approach using decision tree classification (FDTC) to map ISAs and their spatio-temporal changes in a coastal city in southeast China using Landsat 5 TM, Landsat 8 OLI/TIRS, and Sentinel-2 images from 2009 to 2021. Atmospheric correction using simplified dark object subtraction (DOS) was applied to Landsat imagery, which enabled faster computation. FDTC's performance was evaluated with three sensors with different spectral and spatial resolutions, with parameter thresholds held constant across remote-sensing images. FDTC produces a high average overall accuracy (OA) of 94.53%, a kappa coefficient (KC) of 0.855, and a map-level image classification efficacy (MICE) of 0.851 for ISA mapping over the studied period. In comparison with other indices such as BCI (biophysical composition index), PISI (automated built-up extraction index), and ABEI (perpendicular impervious surface index), the FDTC demonstrated higher accuracy and separability for extracting ISA and bare land as well as wetland and high-rise buildings. The results of FDTC were also consistent with those of two open-source ISA products and other remote sensing indices. The study found that the ISA in Xiamen City increased from 16.33% to 26.17% over the past 13 years due to vegetation occupation, encroachment onto bare land, and reclamation of coastal areas. While the expansion significantly reduced urban vegetation in rapidly urbanizing areas of Xiamen, ambitious park greening programs and massive redevelopment of urban villages resulted in a modest but continuous increase in urban green space.

Keywords: urban impervious surface area; coastal city; decision tree classification; land cover; modeling; remote sensing; urbanization



Citation: Hua, L.; Wang, H.; Zhang, H.; Sun, F.; Li, L.; Tang, L. A New Technique for Impervious Surface Mapping and Its Spatio-Temporal Changes from Landsat and Sentinel-2 Images. *Sustainability* **2023**, *15*, 7947. <https://doi.org/10.3390/su15107947>

Academic Editors: Yiyun Chen, Yang Zhang and Zeying Lan

Received: 5 April 2023

Revised: 3 May 2023

Accepted: 10 May 2023

Published: 12 May 2023



Copyright: © 2023 by the authors. Licensee MDPI, Basel, Switzerland. This article is an open access article distributed under the terms and conditions of the Creative Commons Attribution (CC BY) license (<https://creativecommons.org/licenses/by/4.0/>).

1. Introduction

The past 40 years have witnessed significant changes in land use and land cover [1], the most significant of which are characterized by an expansion of impervious surface area (ISA) that replaces the natural vegetation-dominated landscapes [2]. ISA refers to the various impermeable man-made surfaces, such as buildings, roofs, roads, squares, and parking lots, which are mainly constructed from concrete, asphalt, metal, and glass [3]. Given the increasingly concentrated population and high level of economic activity, ISA has emerged as a major indicator of urbanization [4]. Moreover, ISA is an important indicator of environmental quality [5]. In recent years, the worldwide expansion of urban ISAs at an unprecedented rate has resulted in serious urban environmental problems, such as the exacerbation of urban heat islands [6,7], urban heat waves and their related adverse impact on human health [8], increased risk of urban floods [9], and worsening urban water quality including extreme thermal pollution of water bodies [10], all of which combine to alter

biological evolution on a global scale [11]. Consequently, timely and accurate monitoring of ISAs is critical to combat climate change and hydrological cycles and to optimize urban planning, environmental protection, and sustainable urban development [12–14].

Remote-sensing technology offers the advantages of rapidity, accuracy, a synoptic view, repeatable coverage, and a real-time view of large-scale geographic areas, allowing extensive mapping of ISAs and the comparison of multiple, long-term temporal and spatial variations with satellite data [1,3]. Three principal methods exist for estimating ISA: machine learning algorithms, spectral mixture analysis, and spectral index methods. The first group involves machine-learning-based methods, which include decision tree classification (DTC) [15], classification and regression tree [16], support vector machine [17], artificial neural networks [18], deep learning [19], random forest [20], etc. The first group requires high-quality training data, and the second group involves spectral mixture analysis and determines empirical relationships between various spectral and spatial characteristics. The second group also includes linear spectral mixture analysis [21] and multiple end-member spectral mixture analysis [22] and relies heavily on the quality of the endmember, which can be acquired through a complicated process. The last group extracts information from various images based on spectral indices. Numerous ISA spectral indices have been constructed to quantify the biophysical characteristics of the earth's surface, including the normalized difference built-up index [23], the index-based built-up index [24], the urban index [25], the biophysical composition index (BCI) [26], the combinational built-up index [27], perpendicular impervious surface index (PISI) [4], the automated built-up extraction index (ABEI) [28], the normalized difference impervious surface index (NDISI) [29], the normalized built-up area index (NBAI) [30], the built-up area extraction index (BAEI) [31], the enhanced built-up and bareness index (EBBI) [32], the built-up index (BUI) [33], and built-up land features extraction index (BLFEI) [34]. Index-based methods are easy to implement and have acceptable accuracy for many applications [4].

Atmospheric correction strives to obtain precise surface reflectance values by eliminating the influences of the atmosphere, such as scattering and absorption, on remotely sensed imagery. By applying atmospheric correction techniques, these effects can be accounted for, resulting in corrected images that more accurately depict the characteristics and circumstances of the earth's surface. Therefore, this correction is an essential preprocessing step in many remote-sensing applications [35,36]. Atmospheric correction methods can be grouped into three types, i.e., physically based, image-based, and relative calibration methods [34]. The physically based models, such as 6S, LOWTRAN, and MODTRAN, produce very high surface reflectance accuracy. However, the models are highly complicated and require many input parameters obtained from the in situ field atmospheric data received at the time of remote sensing data collection. Image-based models, such as dark object subtraction (DOS) [35] and COST (a particular DOS approach that calculates atmospheric transmittance using the cosine of the solar zenith angle), are implemented through image acquisition and the related header-file information, unlike in situ atmospheric models. The relative correction methods can involve histogram adjustment and dark-pixel subtraction for a single image and image normalization for multi-date images. The third method may be too coarse for applications that require relatively accurate surface reflectance. Therefore, in many remotely sensed applications, DOS is a suitable method to apply, especially when atmospheric data are not readily available for historical image data. However, the original DOS method consists of a series of relatively complex formulas, so simplifying these formulas to one that is easier to apply is highly desirable.

ISA is a typical land cover in cities, and new techniques for mapping ISA have emerged in recent years. Xu [29] used NDISI from Landsat ETM+ images to extract ISAs from the urban area of Fuzhou City, China. Waqar et al. [30] designed NBAI to extract bare soil and built-up area from Landsat 5 TM imagery. Bouzekri et al. [31] applied the built-up area extraction index (BAEI) to extract ISA from Landsat 8 OLI images of Djelfa, Algeria. As-syakur et al. [32] applied EBBI from Landsat ETM+ images to map built-up and bare land areas in Denpasar on Bali Island, Indonesia. To delineate the ISA in Thessaloniki

City, Greece, Kaimaris et al. [33] developed the BUI, which combines the RED, SWIR1, and SWIR2 bands of Landsat ETM+. Bouhennache et al. [34] introduced a built-up land features extraction index (BLFEI) to extract ISA from Landsat 8 imagery in Algiers City, Algeria. Kebede et al. [37] found that NBAI was more accurate than other indices for extracting ISAs from Sentinel-2A data in Addis Ababa, Ethiopia. Finally, Deliry et al. [38] evaluated the supervised object-based nearest neighbor (OB-NN) classification method for extracting urban ISAs from Sentinel-2A data.

Previous studies indicate that the majority of the developed indices can be beneficial for mapping both bare land and ISAs. Nevertheless, some problems remain. For instance, some indices, such as the NDISI and EBBI, require thermal bands, so they are limited to these bands. In addition, it remains difficult in image classification to distinguish between ISAs with spectra that are similar to those of foreign objects (i.e., “salt and pepper”) [19,39] due to the spectral diversity and complexity of urban spatial structures [28]. Some high-albedo objects, such as bare land, and low-albedo objects, such as wetlands and high-rise building shadows in cities, are easily confused with ISA, which reduces the accuracy of ISA extraction [27]. Especially for coastal cities in rapid urbanization, wetlands and high buildings significantly hinder the accurate extraction of ISAs. Therefore, the objective of this study is to (1) simplify the original DOS model for Landsat-5 TM and Landsat-8 OLI images; (2) design an ISA mapping feature approach based on decision tree classification (FDTC) and that integrated multi-feature indices to reduce bare land, vegetation, high-rise building shadows, and wetland interference; (3) explore whether, in a coastal city of China, FDTC can be used with various remotely sensed images with different spatial resolutions and acquired at different seasons; (4) assess the accuracy of the proposed method vis-à-vis other related methods and open-source ISA products (OSPs); and (5) analyze the spatiotemporal variations in ISA and land cover.

2. Study Area

Figure 1 shows that Xiamen City is located in the Fujian Province of China between $117^{\circ}53'$ and $118^{\circ}26'$ East and $24^{\circ}23'$ and $24^{\circ}54'$ North. It is one of the first four special economic zones established in China and obtained many honors, such as “the Habitat Scroll of Honor Award of the United Nations” and “the International Awards for Livable Communities”. It covers a land area of 1700.61 km². The region has a humid subtropical maritime climate characterized by warm temperatures and high humidity throughout the year. The average annual temperature in the area is around 21 °C, providing a comfortable environment for visitors and locals alike. Precipitation levels are also relatively high, with an average of around 1200 mm per year.

The last 30 years have witnessed the rapid urbanization of Xiamen. According to the National Bureau of Statistics of China, by the end of 2021, the permanent population in Xiamen was 5.28 million, which is 4.6 times the population in 1991. Moreover, the gross domestic product of Xiamen increased from 9.77 billion in 1992 to 703.39 billion in 2021.

The study area has transitioned from being a tiny island city to a huge bay-like metropolis. The bay-like city features a city core on the island and four new urban clusters in the bay and plain regions of the mainland [40,41]. Xiamen’s urban spatial pattern is like a huge “hand”, with the sea as the palm, Xiamen Island as the thumb, and the other four districts of Haicang, Jimei, Tong’an, and Xiang’an as four fingers. Although rapid urbanization has brought significant benefits to the residents, it has also caused various environmental problems, including degraded water quality, loss of farmland, rising greenhouse gas emissions, eutrophication of offshore seas, increased flood risks, and enhanced heat-island effects [40,41].

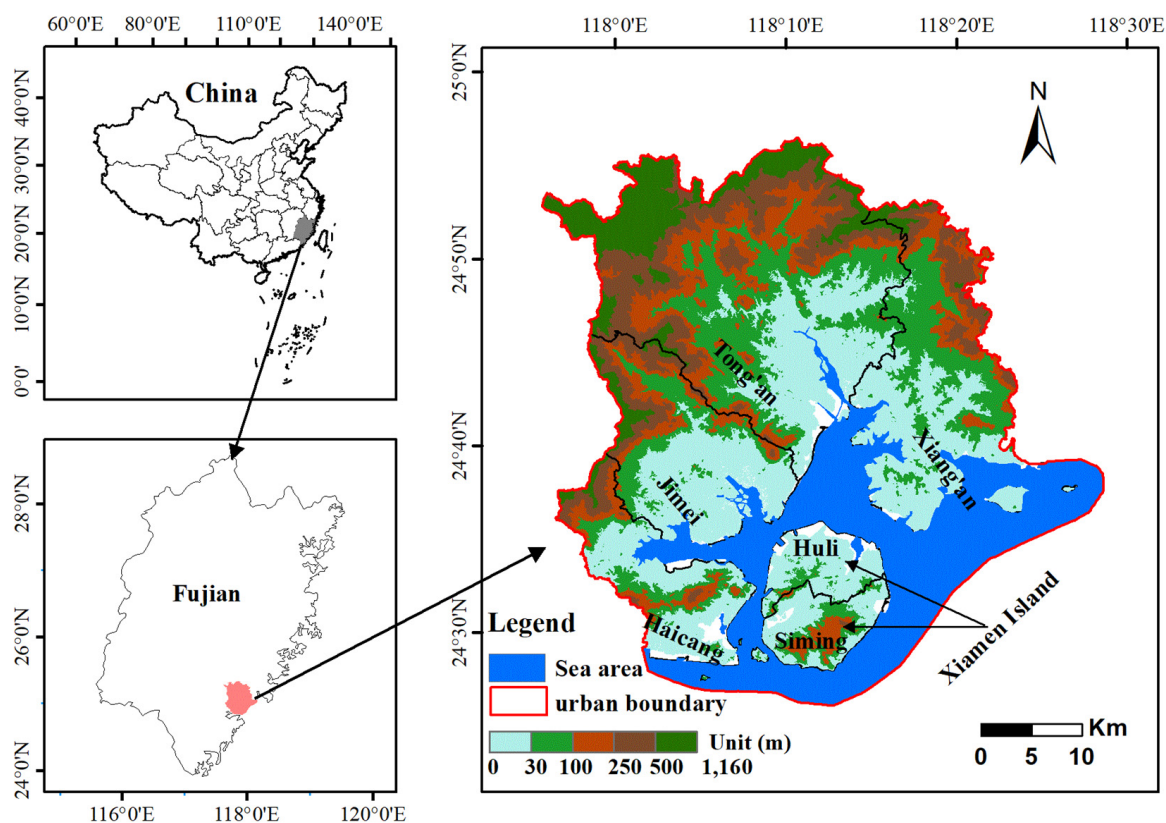


Figure 1. The location of Xiamen City, the study area consisting of four new urban clusters in bays and a central city on Xiamen Island, which is illustrated by the undulating topography.

3. Materials and Methods

Figure 2 shows the research framework, which consists of the following major parts: (1) simplifying the original DOS model; (2) correction of atmospheric effects by using the DOS model with Landsat 5 and Landsat 8, the sen2cor model with Sentinel-2 images, and then creating a remote-sensing database; (3) developing FDTC to mapping ISA and land cover; (4) evaluating the accuracy and comparing with related methods and OSPs; and (5) analyzing variations in ISA and land cover.

3.1. Data Collection and Preprocessing

Five scenes of data acquired with three sensors were downloaded from the website of the United States Geological Survey (<http://earthexplorer.usgs.gov/> (accessed on 10 March 2022)) and the Chinese Geospatial Data Cloud (<http://www.gscloud.cn/> (accessed on 10 March 2022)). The data include one Landsat-5 Thematic Mapper (TM) image, two Landsat-8 images, and two Sentinel-2 images (Table 1). Landsat 8 satellite carries two instruments, the Operational Land Imager (OLI) and the Thermal Infrared Sensor (TIRS). It has one band with 15 m spatial resolution; two thermal infrared bands, 10 and 11, with 100 m spatial resolution; and the remaining bands with 30 m spatial resolution. Sentinel-2 is equipped with a multispectral imager that offers 13 spectral bands with pixel sizes ranging from 10 to 60 m. Among the 13 bands, bands 2–4 and 8 have a spatial resolution of 10 m; bands 1, 9, and 10 have a 60 m spatial resolution; and the remaining bands have a 20 m spatial resolution.

The characteristics of the images utilized in this study are described in Table 1. The images were acquired over different seasons and sun-elevation angles and under clear sky conditions. An atmospheric correction procedure based on the simplified DOS model proposed herein was used to preprocess Landsat-5 and Landsat-8 images.

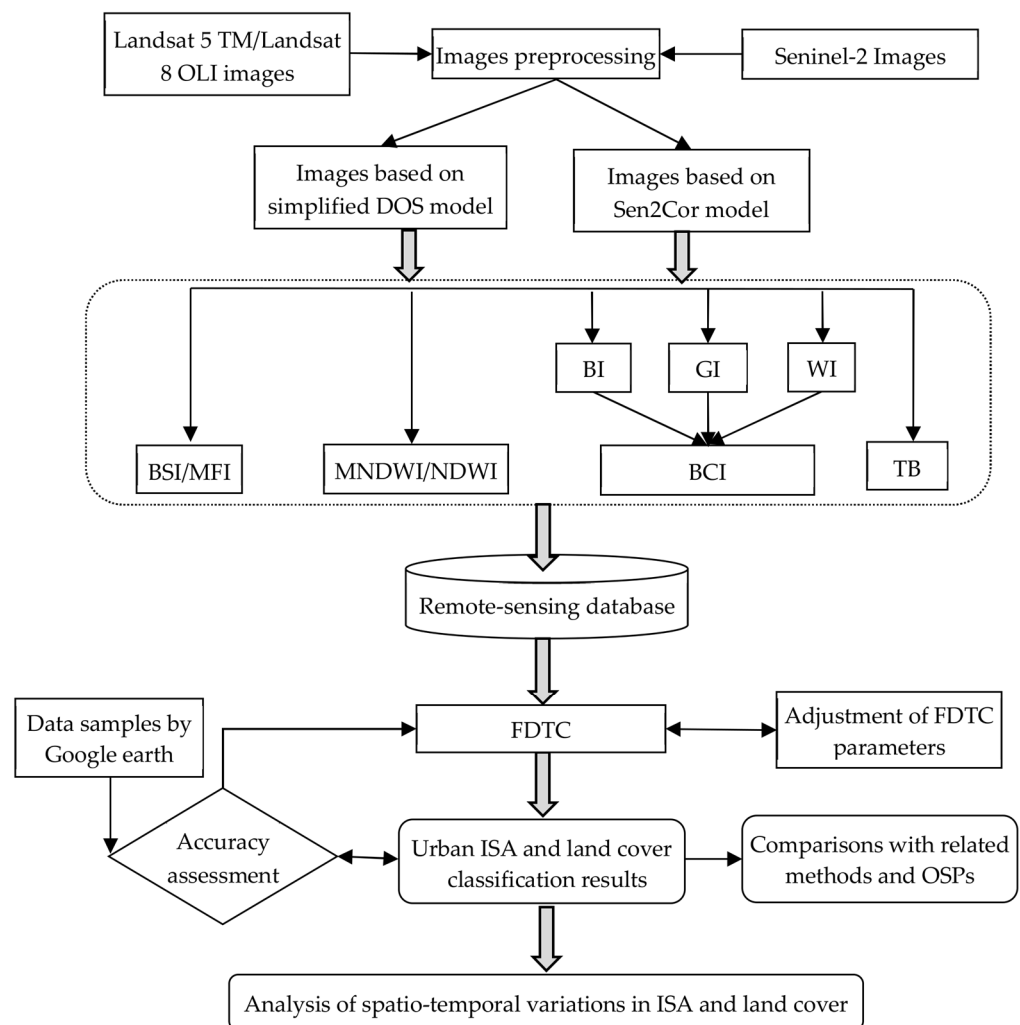


Figure 2. Flow chart showing study procedure. Notes: FDTC is a feature-based approach to decision tree classification; NDWI is the normalized difference water index; MNDWI is the modified normalized difference water index; MFI is the mangrove forest index; BSI is the bare soil index; BCI is the biophysical composition index; GI is the greenness index; BI is the brightness index; WI is the wetness index; TB is the bright temperature. OSPs is open-source ISA products.

Table 1. Description of remote sensing data acquired in Xiamen.

Date	Image Sensor	Sun Azimuth Angle	Sun-Elevation Angle	WRS Path-Row/Orbit-Tile Number
6 June 2009	Landsat 5 TM	89.28	66.34	119-043
11 March 2018	Landsat 8 OLI/TIRS	134.98	52.19	119-043
15 November 2019	Sentinel-2	159.05	42.80	89-T50RPN
15 November 2019	Sentinel-2	157.75	43.14	89-T50RNN
16 December 2021	Landsat 8 OLI/TIRS	154.33	37.61	119-043

Note that the two Sentinel-2 images in Table 1 need be mosaicked to create a complete image encompassing Xiamen City. Sentinel-2 images were preprocessed by using the Sen2Cor atmospheric correction model integrated into the Sentinel Application Platform software (SNAP) [42].

3.2. Image-Based Atmospheric Correction Method

The image-based atmospheric correction method can be divided into top-of-the-atmosphere (TOA) reflectance, DOS, and COST [35,43,44]. Table 2 summarizes the three simplified atmospheric correction methods derived in this study using Landsat 5 and Landsat 8 images.

Table 2. Summary of three atmospheric correction methods for Landsat images.

Name	Landsat 8/Landsat 5	Remark
TOA	$\rho_{TOA} = (M_p \cdot DN + A_p) / \cos \theta$	$K = \pi d^2 / E_0$
DOS	$\rho_{DOS} = M_p (DN - DN_{min}) / \cos \theta + 0.01$	$M_p = K \cdot Gain, A_p = K \cdot Bias$
COST	$\rho_{COST} = M_{COST} \cdot (DN - DN_{min}) / \cos \theta + 0.01$	$M_{COST} = M_p / (TAU_z \cdot TAU_v)$

3.2.1. Simplified Top-of-the-Atmosphere Model

The TOA reflectance (i.e., apparent reflectance) can be expressed as follows:

$$L_{sat} = Gain \cdot DN + Bias, \quad (1)$$

$$\rho_{TOA} = L_{sat} \pi d^2 / (E_0 \cos \theta), \quad (2)$$

where DN is the digital number of the Landsat images, which will be converted to at-sensor radiance; E_0 is the mean exo-atmospheric solar spectral irradiance; θ is the solar zenith angle; d is the astronomical distance between the sun and earth; and $Bias$ and $Gain$ are the coefficients of radiometric bias and gain in a given spectral band, respectively. The coefficients, including d , $Bias$, and $Gain$, can be obtained from the Landsat image header file.

Substituting Equation (2) into Equation (1) yields

$$\rho_{TOA} = \pi d^2 \cdot (Gain \cdot DN + Bias) / (E_0 \cos \theta), \quad (3)$$

Using $K = \pi \cdot d^2 / E_0$, then Formula (3) takes the form

$$\rho_{TOA} = K Gain \cdot DN + Bias / \cos \theta \quad (4)$$

If $M_p = K \cdot Gain$ and $A_p = K \cdot Bias$, then Formula (4) can be simplified into the following formula:

$$\rho_{TOA} = M_p \cdot DN + A_p / \cos \theta \quad (5)$$

USGS revised the Landsat 5 image data processing procedure in 2016. Two extra reflectance parameters (reflectance_mult_band_x and reflectance_add_band_x) are provided in the header file starting in 2016 in addition to the radiance parameters (radiance_mult_band_x and radiance_add_band_x). The two previous radiance parameters correspond to Gain and Bias, respectively. M_p and A_p in equation (5) correspond to the two adjusted reflectance parameters.

For Landsat 8 OLI images, Equation (5) calculates the apparent reflectance. M_p and A_p are also obtained from the header file of Landsat 8 images (i.e., reflectance_mult_band_x and reflectance_add_band_x).

The simplified Formula (5) derived from the original TOA model is very easy to use to obtain the apparent reflectance from Landsat images.

3.2.2. Simplified COST Model

The original COST atmospheric correction model is expressed as

$$\rho_{COST} = \frac{(L_{sat} - L_{haze}) \pi d^2}{E_0 \cdot \cos \theta \cdot TAU_z \cdot TAU_v}, \quad (6)$$

$$L_{haze} = L_{min} - L_{1\%} \quad (7)$$

$$L_{min} = Gain \cdot DN_{min} + Bias, \quad (8)$$

$$L_{1\%} = 0.01 \cdot E_0 \cos\theta \cdot TAU_Z \cdot TAU_V / (\pi d^2), \quad (9)$$

where L_{sat} is the radiation energy received by the sensor ($W/(m^2 \text{ ster } \mu m)$), L_{haze} is the atmospheric path radiance, L_{min} is the minimum spectral radiation value of the remote sensor, and $L_{1\%}$ is the blackbody radiation for each band under the assumption that the blackbody's reflectance is 1%.

For simplification, we define $M_{COST} = \pi \cdot d^2 / (E_0 \cdot TAU_Z \cdot TAU_V) = K / (TAU_Z \cdot TAU_V)$, in which case Equations (6) and (9) can be written, respectively, as

$$\rho_{COST} = (L_{sat} - L_{haze}) \cdot M_{COST} / \cos\theta \quad (10)$$

$$L_{1\%} = 0.01 \cos\theta / M_{COST} \quad (11)$$

Substituting Equations (8) and (11) into Equation (7), we obtain

$$L_{haze} = Gain \cdot DN_{min} + Bias - \frac{0.01 \cos\theta}{M_{COST}} \quad (12)$$

Substituting Equations (2) and (12) into Equation (10) gives

$$\rho_{COST} = \left[Gain \cdot DN + Bias - \left(Gain \cdot DN_{min} + Bias - \frac{0.01 \cos\theta}{M_{COST}} \right) \right] M_{COST} / \cos\theta \quad (13)$$

Equation (13) can be recast as

$$\rho_{COST} = \left[Gain \cdot (DN - DN_{min}) + \frac{0.01 \cos\theta}{M_{COST}} \right] M_{COST} / \cos\theta \quad (14)$$

Further simplifications lead to

$$\rho_{COST} = M_{COST} \cdot (DN - DN_{min}) / \cos\theta + 0.01, \quad (15)$$

where $M_{COST} = M_p / (TAU_Z \cdot TAU_V)$. We have $TAU_V = 1$ since the viewing angle for Landsat TM images is 0° . Two approximate methods were proposed to estimate the atmospheric transmittance TAU_Z , one for the cosine of the solar zenith angle and another for the average of each spectral band derived from the radiative transfer code. However, previous studies demonstrated that the COST model frequently overestimates TAU_V in several applications, especially for clear, cloudless skies with large zenith angles or high northern latitudes. Thus, TAU_V is often ignored in practical applications [45,46].

3.2.3. Simplified DOS Model

When $TAU_V = 1$ and $TAU_Z = 1$, Equation (6) becomes the well-known DOS model:

$$\rho_{DOS} = (L_{sat} - L_{haze}) \pi d^2 / (E_0 \cos\theta) \quad (16)$$

Let $K = \pi d^2 \cdot E_0$ and combine Equation (17) with Equations (11) and (12) to obtain

$$\rho_{DOS} = Gain \cdot K (DN - DN_{min}) / \cos\theta + 0.01, \quad (17)$$

If $M_p = K \cdot Gain$, then we can

$$\rho_{DOS} = M_p (DN - DN_{min}) / \cos\theta + 0.01 \quad (18)$$

3.2.4. Assessment of DOS and Sen2Cor

Compared to raw data, the atmospherically corrected images are visually clearer. It indicates that the atmosphere's effects were removed well in the new images. To quantify the comparison between raw images and corrected images by atmospheric correction, we used the coefficient of variation (CV) as a measure, which was proposed by Yang and Lo [47]. A higher CV value indicates a more dispersed distribution, indicating that the images with larger CV values can lead to better remote sensing classification.

In Figure S1 of the Supplemental File, we included the CV values computed for each band (excluding the thermal band) for different images using atmospheric correction methods. The figure also shows the average of these measures for all bands for each year from 2009 to 2021. For comparison purposes, we computed the same measures for the raw images. As shown in Figure S1, all CV values of corrected images are greater than those of raw images. This suggests that our atmospheric correction methods were very effective in providing important data for subsequent ISA mapping and landcover changes analysis.

3.3. Feature Approach Based on Decision Tree Classification

A decision tree is regarded to be a classification algorithm that uses a binary tree structure to divide a dataset into mutually exclusive subsets based on a set of criteria defined at the root node, as well as numerous internal and terminal nodes (leaves) throughout the tree [15,48]. The interior nodes specify various decision criteria, while the leaf nodes correspond to specific classes. Each internal node has two possible options that split one or more classes from the rest.

DTC offers several advantages, such as wide adaptability, intuitive simplicity, and high computing efficiency. Some DTC approaches (e.g., See5.0, a commercial decision tree algorithm tool [49], and DTC-OOC [50], which is a DTC combined with object-oriented classification) were developed and employed for land cover or thematic information extraction from remote-sensing data. Features can be defined as a series of bands or indices from remote sensing data. In decision tree classification, features act as predictor factors, and the derived land cover classes are the target variables. The determination of target variables is based on a series of criteria and thresholds that take into account the distribution of features in the feature space and other specialized knowledge.

The proposed FDTC method integrates multispectral features acquired from various remote-sensing indices. The indices include the NDWI, MNDWI, BCI, BSI (bare soil index), MFI (mangrove forest index), WI (wetness index), and TB (brightness temperature).

Figure 3 shows the FDTC method for mapping ISA and land cover types based on multiple features. Our research goals and field survey indicate that the land cover classes in the study area can be first categorized as six classes and further merged into four classes. The six classes involve vegetation, ISA, water bodies, bare lands, wetlands, and high-rise building shadows mixed with little roads (HSR). Water bodies include seas, reservoirs, lakes, and rivers. Wetland includes beach land, marshland, ponds, and maricultural areas of the inner bay. When the study area's land cover is examined, the water bodies and wetlands are combined, as are ISA and HSR.

3.3.1. Water Index

McFeeters [51] introduced NDWI as a method to identify open-water features using the green and near-infrared bands:

$$NDWI = (\rho_{Green} - \rho_{NIR}) / (\rho_{Green} + \rho_{NIR}), \quad (19)$$

where for TM/OLI/Sentinel-2 images, ρ_{Green} and ρ_{NIR} represent the spectral reflectances of the green and near-infrared bands, respectively.

Xu [52] proposed the MNDWI index, which can significantly enhance the water information, particularly in areas with mainly built-up land as background. The MNDWI is calculated as follows:

$$\text{MNDWI} = (\rho_{\text{Green}} - \rho_{\text{SWIR1}}) / (\rho_{\text{Green}} + \rho_{\text{SWIR1}}) \quad (20)$$

where for the TM/OLI/Sentinel-2 images, ρ_{Green} and ρ_{SWIR} represent the spectral reflectances of the green and short-wave infrared bands, respectively.

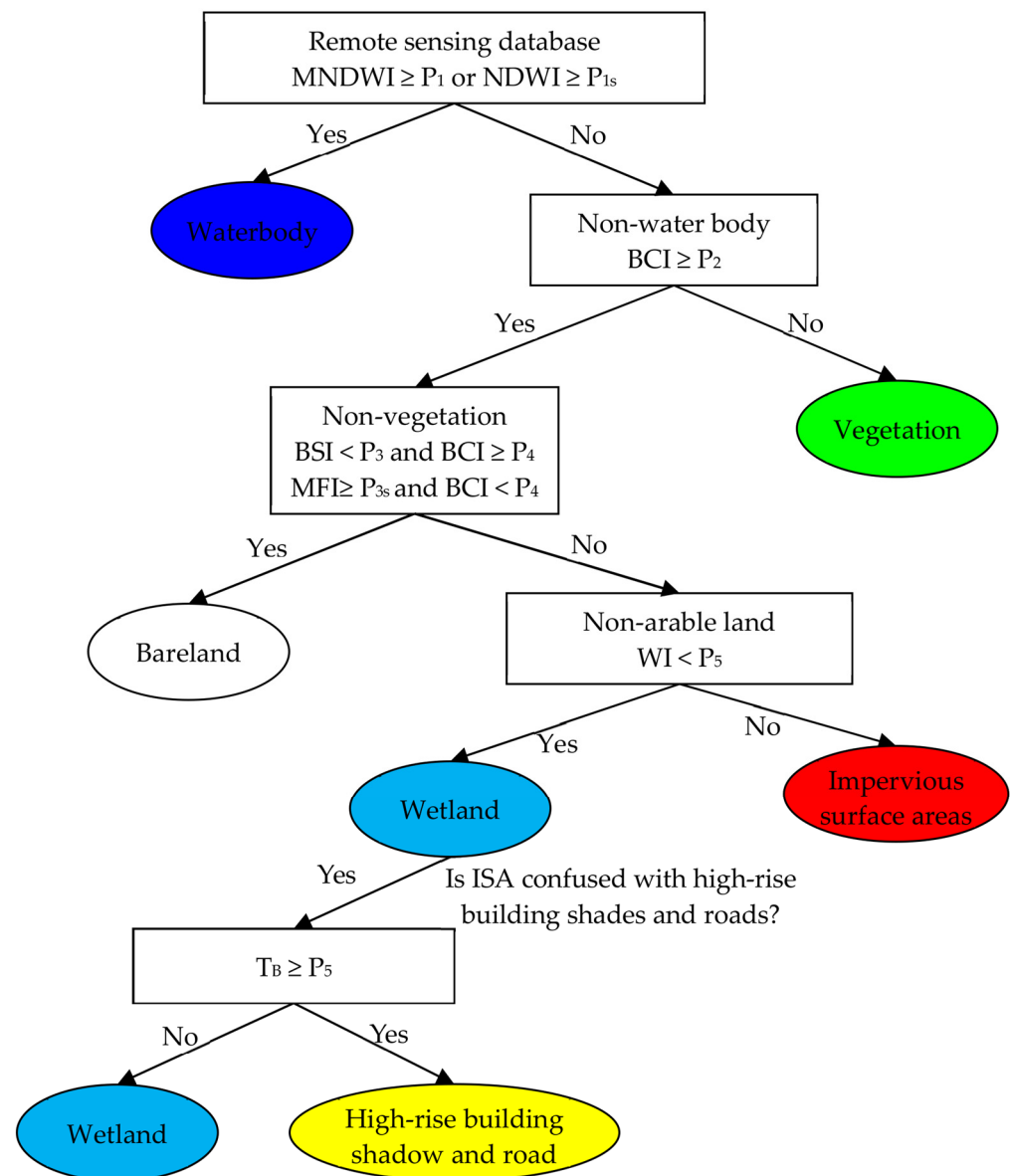


Figure 3. Flow diagram of feature-based approach of decision tree classification for mapping ISA and land cover.

In the Sentinel-2 images, the short-wave infrared band 8 (20 m) and green band 2 (10 m) have different spatial resolutions. The combination of fine-resolution and coarse-resolution images hinders the MNDWI in differentiating spatial details of ecological conditions. The ability of MNDWI to distinguish spectral features of water bodies and non-water bodies in spatial detail would undoubtedly be diminished by combining fine-resolution imagery with coarse-resolution imagery [53].

In addition, for Landsat images with a small solar elevation angle (such as 37.61 in 2021), the high-rise buildings produce spectral features similar to those of water bodies in MNDWI images, unlike NDWI images (Figure 4). Consequently, more high-rise buildings in MNDWI images are misclassified as water bodies. Thus, for Sentinel-2 images or Landsat images with a small solar elevation angle, the NDWI is recommended over the MNDWI.

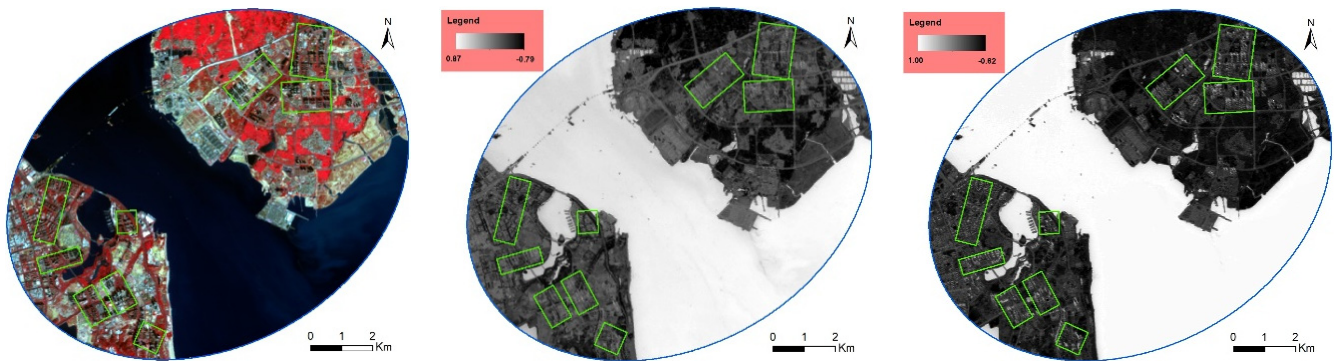


Figure 4. Comparison between Landsat 8 OLI (RGB 543 false color), MNDWI, and NDWI images in 2021. Note: Blue rectangles represent the extent of high-rise buildings.

3.3.2. Bare Land Index

Rikimaru [54] proposed the BSI for bare land, which is expansively used for extracting dust storms in arid areas and bare soil in cities. The BSI is given by

$$BSI = [(\rho_{Red} + \rho_{SWIR1}) - (\rho_{NIR} + \rho_{Blue})] / [(\rho_{Red} + \rho_{SWIR1}) + (\rho_{NIR} + \rho_{Blue})], \quad (21)$$

where ρ_{Red} , ρ_{Blue} , and ρ_{SWIR1} are the spectral reflectances of red, blue, and short-wave infrared (SWIR) 1 bands for TM, OLI, and Sentinel-2 images, respectively.

However, the BSI cannot effectively distinguish ISA from bare land in Sentinel-2 images, so we used the MFI [55] for bare land in Sentinel-2 images. The MFI was proposed for extracting coastal mangroves. However, we found that the index is well adapted to the extraction of bare soil information from Sentinel-2 images when forestland is masked out in the images. The MFI is expressed as follows:

$$MFI = [(\rho_{VRE1} - \rho_{B\lambda 1}) + (\rho_{VRE2} - \rho_{B\lambda 2}) + (\rho_{VRE3} - \rho_{B\lambda 3}) + (\rho_{VRE4} - \rho_{B\lambda 4})] / 4, \quad (22)$$

$$\rho_{B\lambda_i} = \rho_{SWIR2} + (\rho_{Red} - \rho_{SWIR2})(2190 - \lambda_i) / (2190 - 665), \quad (23)$$

where ρ_{VRE1} , ρ_{VRE2} , ρ_{VRE3} , and ρ_{VRE4} are the spectral reflectances of four vegetation red-edge bands in Sentinel-2 images; λ_i is the central wavelength (705, 740, 783, and 865 nm) of each vegetation red-edge band; and $\rho_{B\lambda_i}$ is the reference reflectance of four vegetation red-edge bands.

3.3.3. Impervious Index Based on Biophysical Composition Index

Deng and Wu [26] proposed the biophysical composition index (BCI) in 2012. Its main principle is based on Ridd's triangle-shaped model of vegetation, impervious surface, and soil (V-I-S). To efficiently distinguish ISAs (buildings, roads, etc.) or other impervious features (water, bare land, etc.) from pervious features (e.g., soil and vegetation), the BCI modified the Tasseled Cap (TC) transformation. Deng and Wu [26] concluded that the BCI values for ISA were greater than zero, the vegetation BCI values were less than zero, and the soil BCI values were close to zero. Thus, three components can be distinguished.

These steps can be used to compute the BCI.

$$BCI = [(H + L) / 2 - V] / [(H + L) / 2 + V], \quad (24)$$

where H is high albedo (i.e., the first TC component), V is vegetation (i.e., the second TC component), and L is low albedo (i.e., the third TC component). These three factors are given by the following equations:

$$H = (BI - BI_{\min}) / (BI_{\max} - BI_{\min}), \quad (25)$$

$$V = (GI - GI_{\min}) / (GI_{\max} - GI_{\min}), \quad (26)$$

$$L = (WI - WI_{\min}) / (WI_{\max} - WI_{\min}), \quad (27)$$

where BI , GI , and WI stand for the three TC components of brightness, greenness, and humidity, respectively; BI_{\min} , BI_{\max} , GI_{\min} , GI_{\max} , WI_{\min} , and WI_{\max} are the three TC components' respective minimum and maximum values. In order to obtain the three TC components, linear combinations of the reflected image bands were constructed through TC transformations. For the TM, OLI, and Sentinel-2 images, the TC transformation reflectance coefficients were acquired from Crist [56], Baig et al. [57], and Shi and Xu [58], respectively.

3.3.4. Brightness Temperature (TB)

TB defines the temperature of a black body radiator at the same radiance [59]. TB is obtained from Landsat 5, Landsat 8 satellite's thermal-infrared data, using the following equation:

$$TB = k_2 / \ln(1 + k_1 / L_\lambda), \quad (28)$$

where k_1 and k_2 represent two constants of thermal bands from image header files, band 6 for Landsat 5 and band 10 for Landsat 8. For Landsat 8, $k_1 = 774.89 \text{ W m}^{-2} \text{ sr}^{-1} \mu\text{m}^{-1}$, $k_2 = 1321.08 \text{ K}$; for Landsat 5, $k_1 = 607.76 \text{ W m}^{-2} \text{ sr}^{-1} \mu\text{m}^{-1}$, $k_2 = 1260.56 \text{ K}$. L_λ is the radiance at the satellite (i.e., top of the atmosphere).

3.3.5. The Principle of FDTC

As seen in Figure 3, MNDWI or NDWI are applied to assign each image into one of two groups because water bodies have much higher MNDWI and NDWI values than other types of land cover. Previous studies demonstrate that setting an initial threshold of zero for the NDWI or MNDWI can generally allow most water bodies to be distinguished from other land-cover types.

The BCI can be used to distinguish between vegetated (such as forests and crops) and non-vegetated environments (built-up land, bare land, and beaches) because non-vegetation areas have higher BI values compared with vegetation areas (Figure 5).

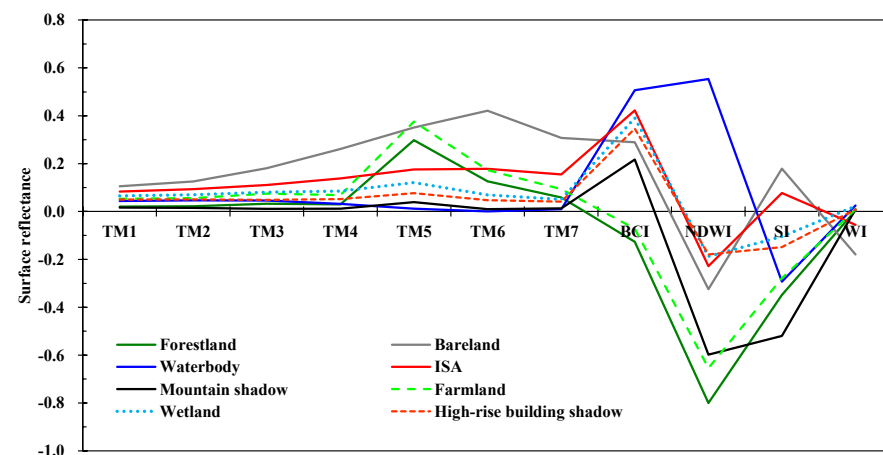


Figure 5. Spectral response curves of various land-use and land-cover types in Xiamen City in 2021.

The BSI is useful for separating bare land from ISA because the former corresponds to a greater BSI value than that of ISA. However, the BSI does not work well with Sentinel-2 imagery. Therefore, the BSI was replaced by the MFI for Sentinel-2 imagery.

The WI is useful for differentiating wetlands from ISAs because wetland has a higher WI than ISA. However, roads and shade from high-rise buildings on ISA appear similar to wetlands in the WI spectra in Figure 5. Roads and high-rise buildings usually absorb heat in the daytime and become warmer than wetlands. Thus, TB is used in combination with WI to distinguish between wetlands and ISAs.

3.3.6. The Calibration of FDTC Parameters

After all the images underwent atmospheric correction using the DOS or Sen2Cor method, a dataset for each feature band, including NDWI (or MNDWI), BSI (or MFI), BCI, WI, and TB bands, were produced. To train each landcover class for Landsat or Sentinel-2 images from 2009 to 2021, we utilized a minimum of 15 training sites per period. These sites were obtained by using Google Earth (GE) images that were as close in date as possible to the original remotely sensed data, with sizes ranging from 16 to 600 pixels. To obtain the initial set of FDTC parameters, we calculated a minimum pixel value in each feature band (BCI, etc.) for training sites containing the corresponding landcover class. The histograms for each feature band (such as NDWI and BCI) facilitate the separation of the pairing landcovers (such as waterbody and non-waterbody) in Figure 3. As a threshold value, the point in the histograms where the two classes separate was chosen [37]. Therefore, the initial parameters may be adjusted and combined with the histograms to analyze the study area. Where necessary, we further reviewed and adjusted the parameters based on the accuracy of the landcover classes.

3.4. Accuracy Assessment

Accuracy assessments are crucial to evaluate the performance of various image classifications or specific feature extractions. Due to unavailable ground data for historical remote-sensing data, we used independent ground samples from GE images as reference data in this investigation. The dates of the GE images we selected (29 October 2009, 10 March 2018, 23 August 2020, and 27 July 2021) were as close to those of the original images as feasible in order to obtain the best reference data.

We randomly selected 910 samples for each scene using a stratified random sampling scheme, with at least 60 samples for each class. These samples were exported to GE for accuracy assessment, and the classification results were evaluated using a confusion matrix.

In this study, three validation metrics, kappa coefficient (KC), overall accuracy (OA), and map-level image classification efficacy (MICE), were applied. An OA value greater than 70% is recognized as satisfactory [60], and a Kappa value above 0.8 indicates strong agreement (beyond chance) [61]. Shao et al. [62,63] pointed out that the accuracy metric kappa has two significant disadvantages: being extremely sensitive to class imbalance and lacking explicit interpretations for evaluating classification performance. To overcome the shortcomings of the evaluation metric, the metric MICE was introduced to estimate image classification. An Excel template is very helpful for obtaining MICE (see <https://web.ics.purdue.edu/~shao/> (accessed on 8 September 2022)). The MICE is expressed as follows:

$$\text{MICE} = (A - A_0) / (1 - A_0), \quad (29)$$

where A_0 represents the accuracy of a random classification used as a baseline, and A is the overall accuracy.

In order to compare the performance of the proposed FDTC with those of other indices, the three indices BCI, ABEI, and PISI were applied for the four images with three sensors, leading to various ISA maps.

The ABEI was proposed based on Landsat 8 OLI reflective bands [28]. ABEI can distinguish built-up areas from bare land, sand, and rock. The ABEI is given as

$$ABEI = 0.312Ref_1 + 0.513Ref_2 - 0.086Ref_3 - 0.441Ref_4 + 0.052Ref_5 - 0.198Ref_6 + 0.278Ref_7 \quad (30)$$

where Ref_1 – Ref_7 represent the spectral reflectance of coastal, blue, green, red, near-infrared, and two short-wave infrared (SWIR1 and SWIR2) bands for Landsat 8 OLI images, respectively. Note that the ABEI is limited to Landsat 8 OLI images. Additionally, the ABEI must first set $NDVI < 0$ and $NDVI > 0.5$ to exclude pure pixels of vegetation and water.

The PISI was proposed [4] based on the spectral reflectance in the blue and near-infrared bands, which can be applied to various images. The PISI is given as

$$PISI = 0.8192\rho_{Blue} - 0.5735\rho_{NIR} + 0.0750, \quad (31)$$

In addition, we also compare our results with two open-source ISA products (OSP). The open-source datasets, namely global artificial impervious area (GAIA) [64] with 30 m resolution and Dynamic world (DW) [65] with 10 m resolution, were used as validation data because they were all created primarily from Landsat or Sentinel-2 images acquired over short time intervals and with good spatial resolution and high accuracy. We implemented change detection between the FDTC and each ISA product to obtain common regions. The common region defines pixels whose classification (ISA or non-ISA) is consistent, which are typically regarded as accurate pixels [66]. We defined the following formulas to evaluate the accuracy of ISA or non-ISA in the common region between FDTC results and each ISA product.

$$A_{ISA} = ISA_C / ISA_F \times 100\%, \quad (32)$$

$$A_{NISA} = NISA_C / NISA_F \times 100\%, \quad (33)$$

where A_{ISA} and A_{NISA} represent the percent accuracy of ISA and non-ISA; ISA_C represents the area of a common region of ISA between FDTC result and each ISA product (GAIA or DW); ISA_F represents the total area of ISA obtained by FDTC; $NISA_C$ represents the area of a common region of non-ISA between FDTC result and each ISA product; $NISA_F$ represents the total area of non-ISA obtained by FDTC.

4. Results and Discussion

4.1. Parameter Analysis for FDTC

Extraction of ISA and land cover was carried out using FDTC based on the multiple-feature dataset consisting of NDWI or MNDWI, BCI, BSI or MFI, WI, and TB. The parameter values obtained from the dataset spanning from 2009 to 2021 are presented in Table 3. Some FDTC parameters were relatively stable, and others varied only slightly, except for TB. Given the significant effects of season and climate change on surfaces, the surface temperature varies greatly. We found that the TB calculated from winter images has difficulty distinguishing water bodies, roads, and building shadows. Therefore, in the years 2019 and 2021, we used summer TB images to replace winter TB images (September 2019 and July 2021, respectively). The threshold of the water parameter (i.e., MNDWI or NDWI) is approximately zero, and the water parameter for Sentinel-2 images is higher than that for Landsat images. The threshold of the ISA parameter (BCI) can range from 0.05 to 0.14 due to different sensors and seasons. The WI varies from 0 to -0.16 due to different sensors and various ocean tides caused by lunar gravity.

Table 3. Parameters of FDBC derived from three sensors in Xiamen.

Sensor Type	Year	MNDWI/ (P_1)	NDWI (P_{1s})	BCI (P_2)	BSI and BCI (P_3 and P_4)	MFI and BCI (P_{3s} and P_4)	WI (P_5)	TB(P_6)
Landsat-5	2009	-0.05	/	0.13	0.17 and 0.75	/	-0.10	301.00
Landsat-8	2018	0	/	0.06	0.15 and 0.4	/	-0.04	292.86
Sentinel-2	2019	/	0.09	0.05		0.25 and 0.4	-0.15	299.70
Landsat-8	2021	/	0.02	0.14	0.13 and 0.4		0	299.80

Figure 6 shows the land cover map covering the northeast of Xiamen Island, Xiang'an new town, and their adjacent sea area using the FDTC. The FDTC effectively separates ISA from bare land by using the BCI and the BSI or MFI. It uses WI combined with BT to distinguish wetlands from ISA and high-rise buildings.

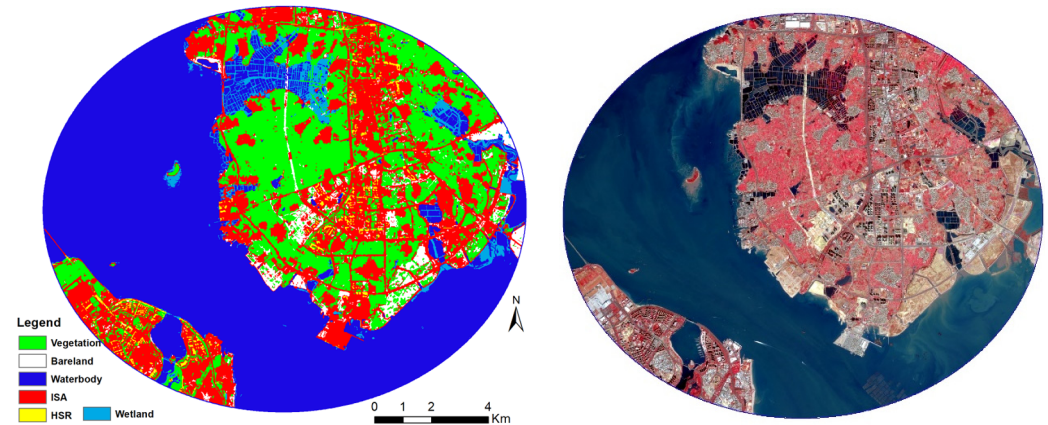


Figure 6. Comparison of Sentinel-2 image (RGB 843 false color) with land cover using FDTC method. Data were acquired in 2019. Note: HSR is high-rise building shadows mixed with little roads.

Due to rapid urbanization, more high-rise buildings have sprung up (Figure 7). Far more high-rise buildings appeared after 2019 than in 2009. Compared with two 30 m land cover images for both the 2009 Landsat 5 TM and 2021 Landsat 8 images, FDTC produces a 10 m land cover image for the Sentinel-2 image and thus significantly improves the spatial details of the land cover. For ISA and land cover studies on an urban scale, higher spatial resolution is always desired. A fine-scale map with intricate spatial details allows urban planners to understand and examine how ISA structures and urban land cover affect living conditions. Therefore, Sentinel-2 images should play a more important role in the study of urban ISA and land cover in the future.

4.2. Analysis of Classification Accuracy for ISA

Figure 8 displays the OA, KC, and MICE of ISA maps generated using FDTC and the other three methods applied to four-period images. The FDTC method achieves higher OA values of 94.40%, 93.41%, 95.05%, and 95.27% in 2009, 2018, 2019, and 2021, respectively, compared to BCI (85.16–85.71%) and PISI (87.25–88.90%), as well as ABEI (88.13–90.02% in 2018 and 2021). KC and MICE values are also higher for FDTC results than those obtained from other methods. MICE values are usually smaller than KC values due to their ability to handle class-imbalance effects [62]. For instance, while the KC value is 0.675 for BCI in 2021, MICE yields a lower value of 0.640.

The FDTC method produces a high average OA of 94.53%, a KC of 0.855, and a MICE value of 0.851. The average OA increases by 9.93%, 7.58%, and 6.20% compared with the corresponding values for BCI, PISI, and ABEI. The average KC values increase by 0.212, 0.183, and 0.151 compared with those for BCI, PISI, and ABEI. The average MICE values increase by 0.256, 0.190, and 0.160 compared with those for BCI, PISI, and ABEI. Therefore, compared to the other three indices, the proposed technique yields more accurate results.

Figure 9 shows spatiotemporal changes in ISA maps obtained from the FDTC and other indices. The other three indices are mislabeled as ISA large areas of bare land and wetland. Furthermore, many hill shadows are mislabeled as ISA (Figure 9i) by the PISI method since the sun elevation angle is smaller in 2021 than that in other years. This shows that when using the PISI method in images with a smaller solar elevation angle, its accuracy may be impacted. Further data are needed to verify this notion.

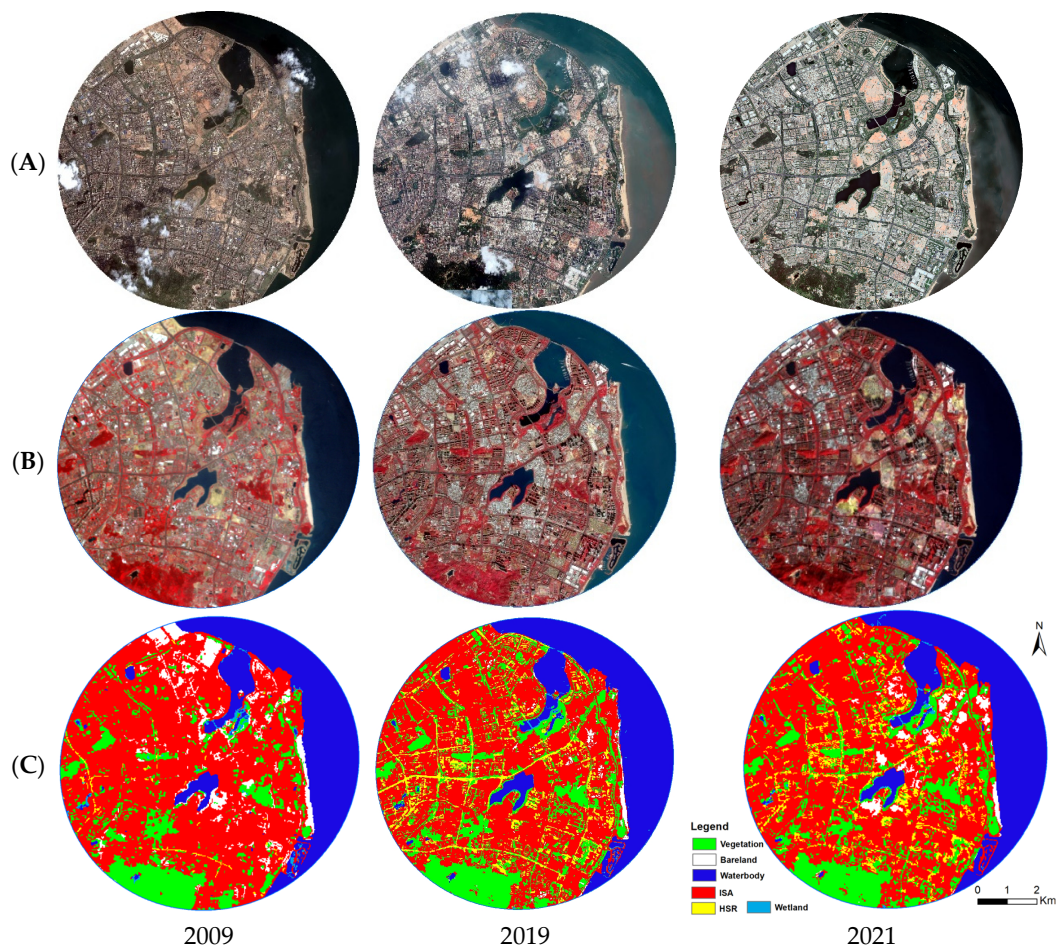


Figure 7. Comparison between (A) Google Earth images, (B) Landsat 5 TM/Landsat 8 OLI/Sentinel2 images (RGB false color), and (C) corresponding land cover maps made using FDTC method. Image shows eastern Xiamen Island.

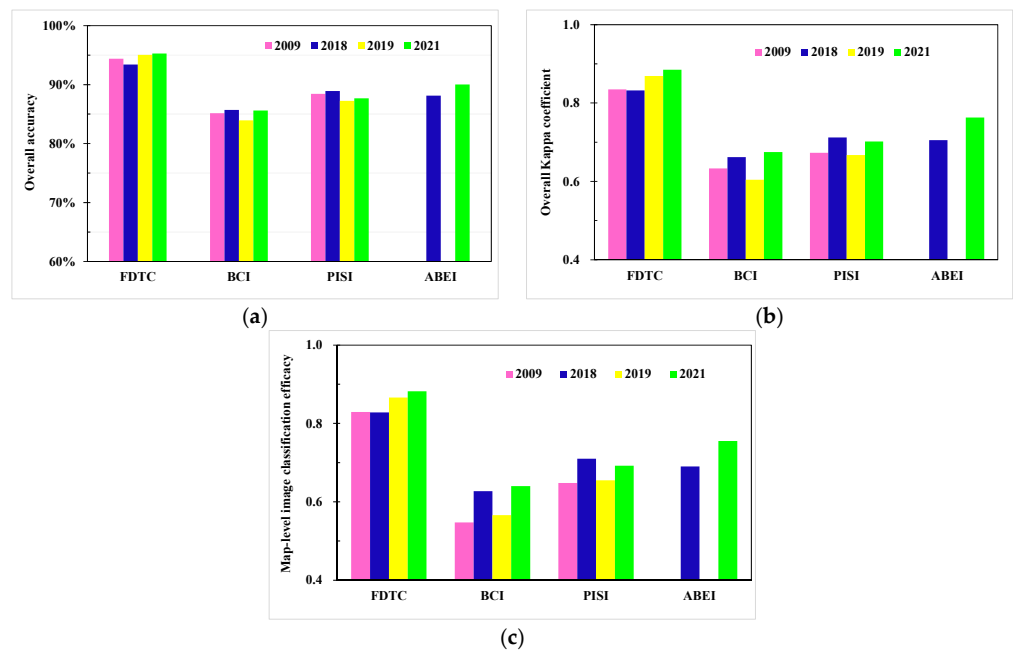


Figure 8. Comparison of ISA classification accuracy by OA (a), KC (b), and MICE (c) using different methods from 2009 to 2019.

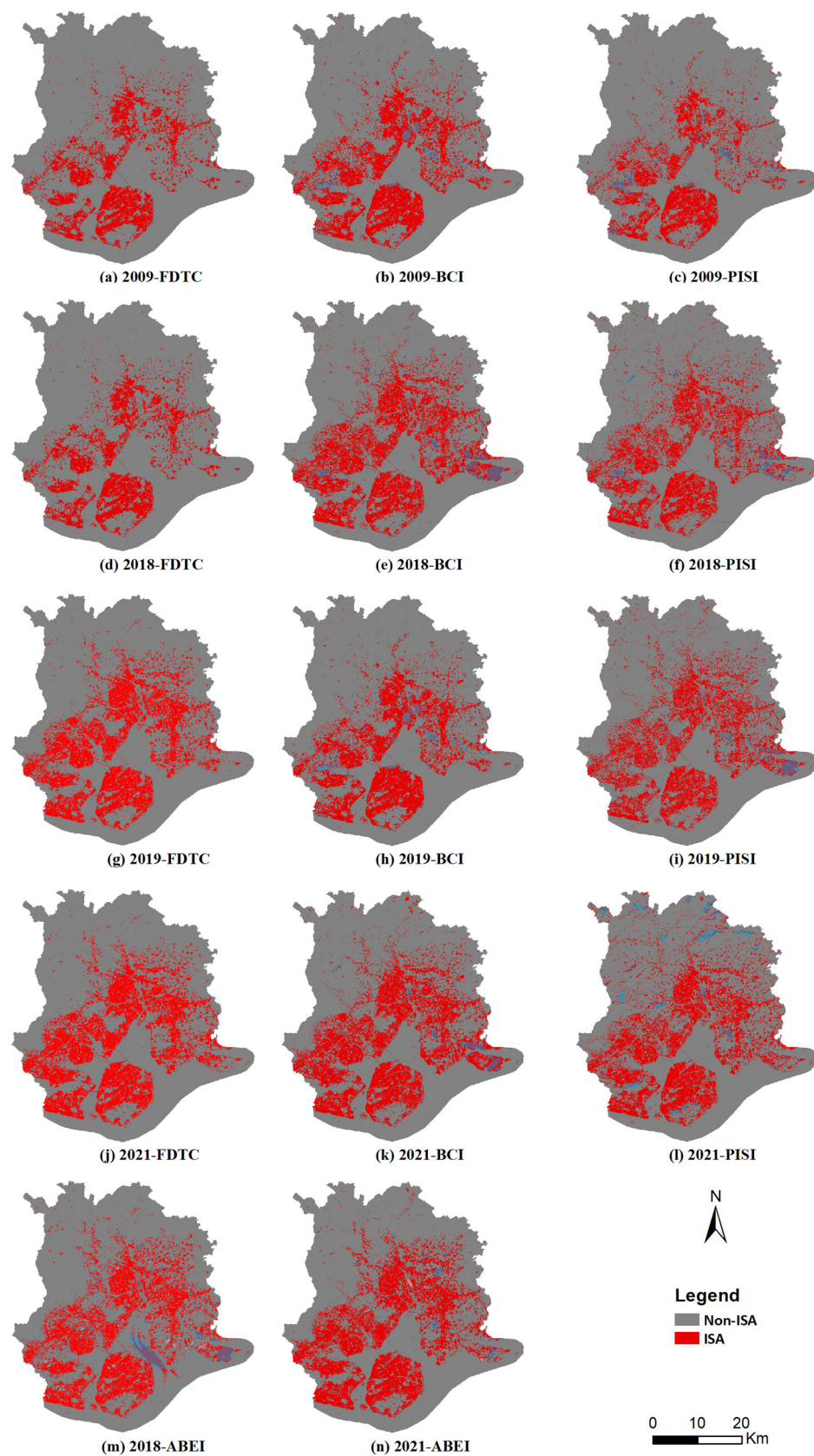


Figure 9. Comparison of ISA extraction results for different methods using three sensors from 2009 to 2021 in Xiamen. Note: Blue eclipses represent the regions where ISA is significantly misclassified.

For all images, the accuracy obtained by the FDTC exceeds that obtained by the other methods. The FDTC method displayed high accuracy stability in four images with diverse surfaces and environmental conditions compared to other methods, as confirmed by the accuracy assessment results.

4.3. Comparison of ISA Classification Accuracy with Related Methods

Table 4 compares our results with those of previous studies using various indices. Tian et al. [26] used PISI to map the ISA distribution in four cities in China and estimated an average OA of 93.40% and a KC of 0.87. Firozjaei [28] used data from Landsat 8 and ABEI to generate an OA of 88.46% and a KC of 0.87. Xu [29] obtained an ISA map based on NDIS and achieved an OA of 90.70% and a KC of 0.81. Waqar et al. [30] applied NBAI to extract ISA and reported an average OA of 86.87% and a KC of 0.73. Bouzekri et al. [31] prepared an ISA map-based BAEI and achieved an OA of 92.66% and a KC of 0.85 for Landsat 8. Kaimaris et al. [33] delineated the ISA map using Landsat ETM+ and BUI method and estimated an OA of 90% and a KC of 0.8. Bouhennache et al. [34] prepared an ISA map using BLFEI and estimated an OA of 95% and a KC of 0.9 for Landsat 8. For Sentinel-2 and Landsat-8 images, Deliry et al. [38] developed the OB-NNC method and obtained an OA of 90.91% and 88.64% and a KC of 0.82 and 0.77, respectively. Therefore, the results obtained by FDTC compare well with those obtained from other remote sensing indices.

Table 4. Comparisons of ISA classification accuracy with other related studies.

Authors	Methods	Sensors	OA%	KC
Tian et al. [4]	PISI	Landsat 8	89.51~96.50	0.79~0.93
Xu [29]	NDISI	Landsat ETM+	90.70	0.81
Firozjaei et al. [28]	ABEI	Landsat 8	92.04~97.62	0.90~0.96
As-syakur et al. [32]	EBBI	Landsat ETM+	88.98	/
Kaimaris et al. [33]	BUI	Landsat ETM+	90	0.8
Waqar et al. [30]	NBAI	Landsat 5 TM	86.87	0.73
Kebede et al. [37]	NBAI	Sentinel-2	93~97	0.86~0.92
Bouhennache et al. [34]	BLFEI	Landsat 8	95	0.9
Bouzekri et al. [31]	BAEI	Landsat 8	92.66	0.85
Deliry et al. [38]	OB-NNC	Sentinel-2	90.91	0.82
		Landsat 8	88.64	0.77
Hua et al. (this study)	FDTC	Landsat 5 TM	94.40	0.84
		Landsat 8	93.41~95.27	0.83~0.89
		Sentinel-2	95.05	0.87

4.4. Comparison with Open-Source ISA Products

Table 5 compares the percent accuracy from our classification results with those of the two open-source ISA products (GAIA and DW). In the common regions between the FDTC and each ISA product, the average A_{ISA} and A_{NISA} are 86.25% and 90.41%, respectively. The analysis reveals that our results are entirely consistent with currently published ISA products (Figure 10).

Table 5. Percent accuracy between classifications achieved by FDTC and open-source ISA products in common regions.

Year	ISA Product Type	A_{ISA} (%)	A_{NISA} (%)
2009	GAIA	73.25	98.54
2018	GAIA	80.47	96.81
2019	DW	91.91	82.89
2021	DW	99.37	83.41
	Average	86.25	90.41

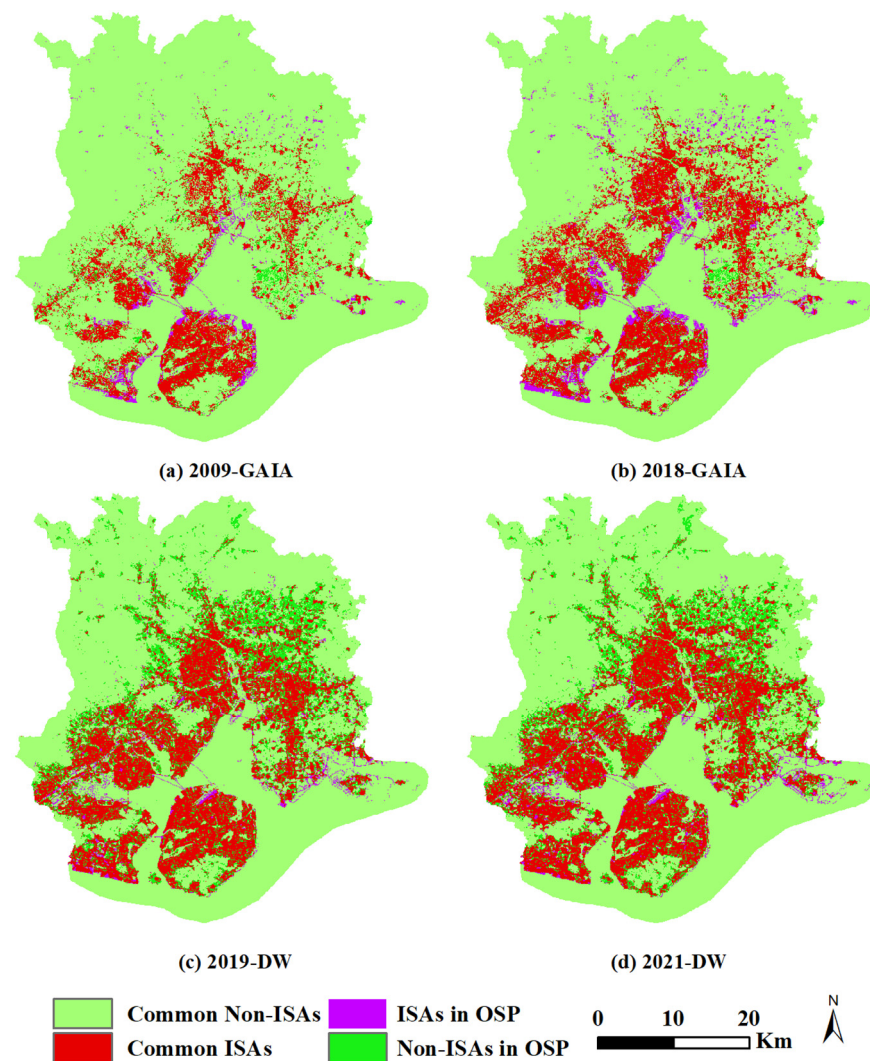


Figure 10. The ISA maps showing for two open-source ISA products (OSPs): GAIA and DW, from 2009 to 2021.

Figure 10 displays unique distinctions between our classifications and two open-source products due to the various classification techniques. The area mapped ISA with GAIA is slightly less than our results (Figure 10a,b). Many pixels that should be fallow ISAs generated by coastal reclamation in the study area were divided into non-ISAs in GAIA. However, the area mapped ISA with DW is considerably larger than our results (Figure 10c,d). Many pixels that should be vegetation areas with low coverage (e.g., fallow land) in the study area were misclassified as ISAs in DW. The analysis showed that the FDTC could achieve results similar to open-source ISA products, proving the feasibility of the proposed method.

4.5. Analysis of Classification Accuracy for Land Cover

Table 6 summarizes the accuracy assessment for land-cover classification based on the FDTC. The overall accuracy of the four-period land cover maps using the FDTC method ranges from 90.77% to 92.74%. Both KC and MICE vary from 0.865 to 0.895 (Table 6). The average OA, KC, and MICE values are 91.54%, 0.877, and 0.877, respectively. The three metrics of classification assessment indicate that the classification is reasonable for real-world image classifications.

Table 6. Summary of land-cover accuracy using FDTC from 2009 to 2021.

Sensors	Date	OA (%)	KC	MICE
Landsat 5 TM	June 2009	91.10	0.869	0.869
Landsat 8 OLI	March 2018	90.77	0.865	0.865
Sentinel-2	November 2019	91.54	0.879	0.879
Landsat 8 OLI	December 2021	92.74	0.895	0.895

Note: OA is overall accuracy; KC is overall kappa coefficient; MICE is map-level image classification efficacy.

4.6. Spatiotemporal Land-Cover Changes

The study region's land cover distributions and area percentages from 2009 to 2021 are depicted in Figures 11 and 12, respectively. Over the last 13 years, ISA saw the most significant increase among the four land-cover classes, rising from 16.33% to 26.17%. The urban ISA expansion was predominantly achieved by occupying vast areas of vegetation, encroaching upon bare land, and reclaiming coastal regions. Vegetation decreased the most over the study period, from 57.76% to 51.37%. Since the majority of forestland can be concentrated in hilly regions that are unfavorable for urban ISAs, farmland is primarily losing vegetation rather than forestland in Xiamen. Water bodies and beaches experienced the second-largest decrease, from 23.55% to 20.64%. A “cross-island development” strategy that was implemented to encourage the transformation of Xiamen from a tiny island city to a huge bay-like metropolis may be the main cause of the decrease in water bodies and wetlands [67].

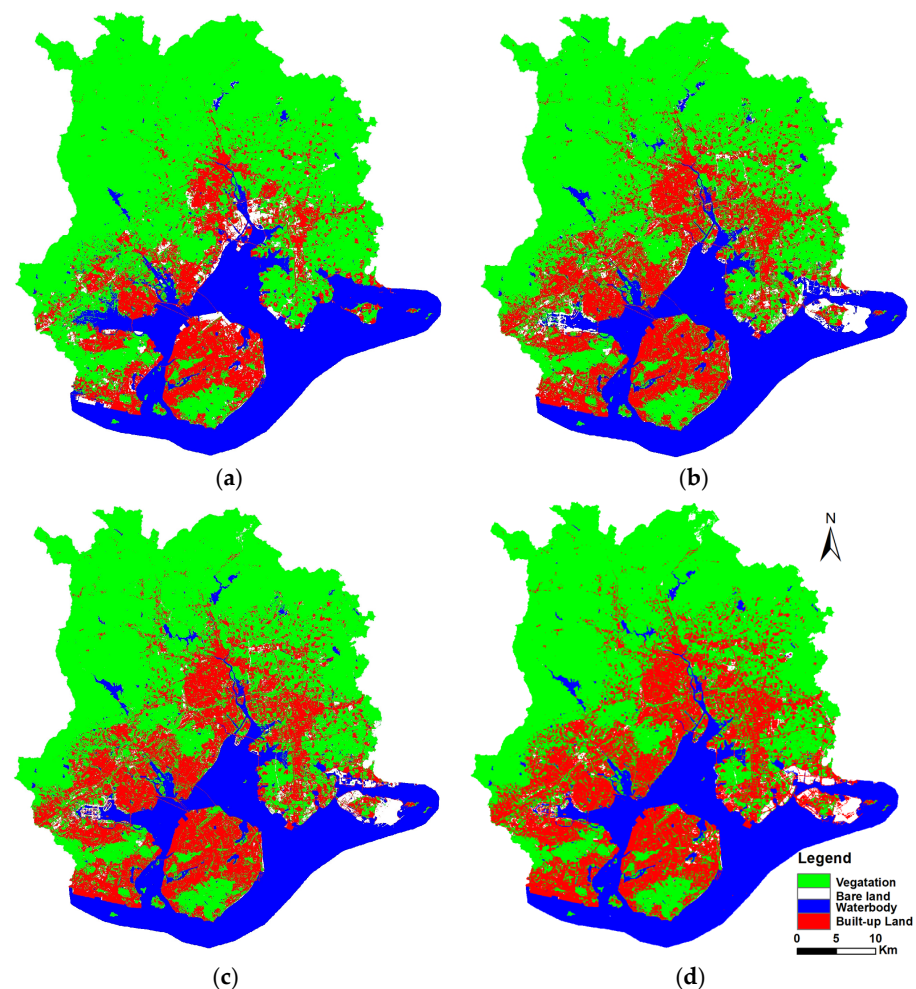


Figure 11. Land cover classification results based on the feature-based approach of decision tree classification (FDTC) applied to various images: (a) Landsat 5 image from 2009; (b) Landsat 5 image from 2018; (c) Sentinel 2 image from 2019; (d) Landsat 8 image from 2021.

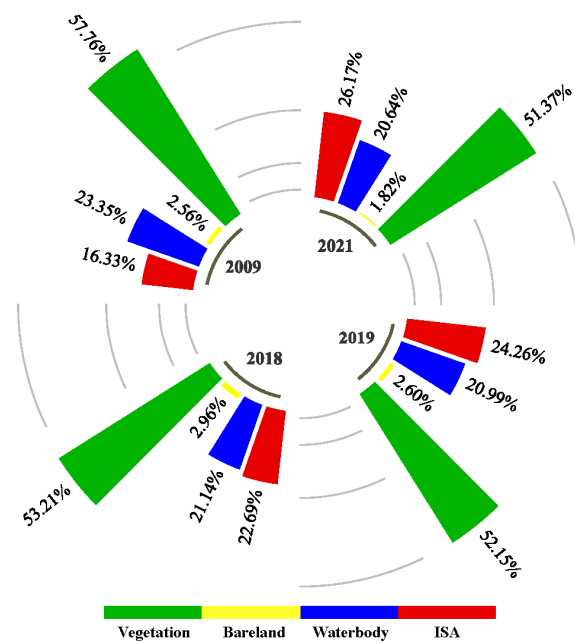


Figure 12. Land cover changes in the study area from 2009 to 2021.

Bare land is an important land-use type. The total area of bare land monitored in Xiamen was 56.33 km² in 2009, accounting for 2.56% of the total area of Xiamen. In 2021, the percentage dropped to 1.81%. Figure 7 shows that four urban villages changed from ISA (Figure 7—2019C) to bare land (Figure 7—2021C) in the Huli district. The bare land is viewed as a source of dust pollution because fine particles of bare soil are easily transported into the atmosphere by the wind and then cause air pollution. The local government has taken important measures (“blue sky defense battle”) to control dust pollution and continue to improve the ambient air quality. For example, the bare land in the construction areas can be temporarily covered with dust-proof nets (green plastic nets), and the long-term reserve lands may be planted with suitable green vegetation.

4.7. Spatiotemporal ISA Changes

Figures 13 and 14 show significant changes in ISA expansions in Xiamen from 2009 to 2021. The results show that the ISA increased dramatically over the study period from 318.95 km² in 2009 to 511.11 km² in 2021, representing a 0.60-fold increase over the past 13 years (Figure 13), or an average annual increase of 14.78 km²/year. The rates of increase in ISA in the two stages differ. In the first stage, the increase in ISA occurs between 2009 and 2018, when the ISA grows by 124.20 km², for an average annual increase of 13.80 km²/year. In the second stage, the average annual increase in ISA between 2018 and 2021 exceeds that in the first stage by reaching 16.99 km²/year.

Figure 14 revealed that the boost in ISA in Xiamen from 2009 to 2021 was achieved at the expense of natural resources such as vegetation, water bodies, and bare land. A significant portion, specifically 71.75%, of the newly developed ISA was taken from vegetated areas, resulting in a loss of more than 12.98 km² of vegetated land per year. Additionally, 14.01% of the new ISA was obtained from converting water bodies, primarily sea areas abutting the land, while 14.23% came from converting bare land.

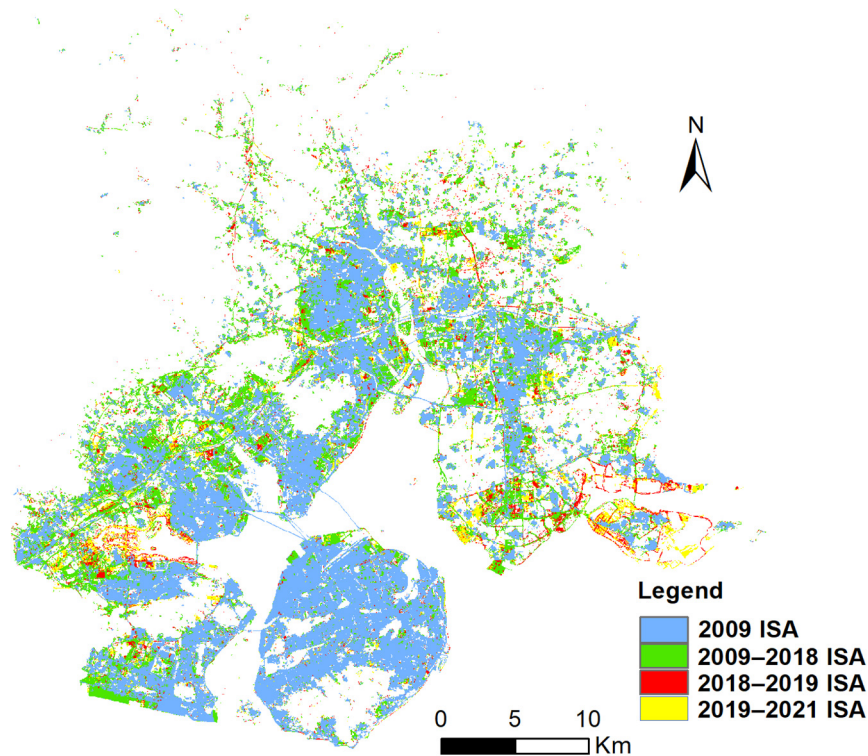


Figure 13. Impervious surface area (ISA) growth in four stages from 2009 to 2021 in Xiamen City.

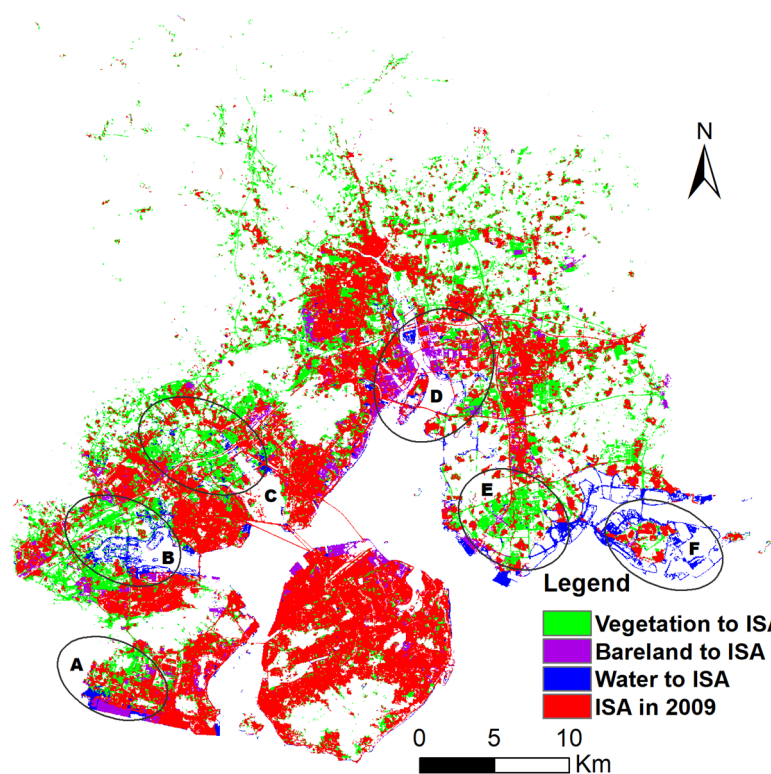


Figure 14. ISA (impervious surface area) conversion from water, vegetation, and bare land between 2009 and 2021 in Xiamen City. Note: A—Haicang Bay, B—Maluan Bay, C—Xinling Bay, D—Tong'an Bay, E—Xiang'an new urban area, F—Xiamen second international airport under construction.

The surrounding areas of Haicang Bay, Malyuan Bay, Xinglin Bay, Tong'an Bay, Xiang'an new urban areas, and the second airport of Xiamen witnessed the most significant increase in ISA (Figure 14). The ISA increase in Xiamen is characterized by the bay-like

form of the city. Two main reasons may explain this urban pattern: Firstly, the ISA sprawl is constrained by the coastal line. Secondly, to alleviate population pressure on Xiamen Island, a novel policy called “the cross-island development strategy” was implemented in 2002 to guide the excessive population on Xiamen Island to the mainland. Four new urban areas located in four bays (Haicang Bay, Maluan Bay, Xinling Bay, and Tong’an Bay) witnessed rapid population growth, strong economic growth, and a rapid increase in ISA increase. The four new urban areas accounted for about 47.29% of the total population in Xiamen in 2010, and the percentage reached about 60.47% at the end of 2021. What is remarkable is that Jimei District tops the list for the first time with 1.078 million people in 2021, accounting for more than 20% of the total population in Xiamen.

According to Figure 14, the second airport in Xiamen is well in progress. The new airport, located on Dadeng Island of the Xiang’an District, is a rare island-type airport and an important international cargo port. The land-reclamation area of the airport will be approximately 8.23 km². The project has two phases. It will be a 4F-level airport that can handle various large aircraft and have an annual passenger throughput of 45 million in the first phase and 85 million in the second phase.

Coastal reclamation is one of the most crucial strategies for supplying land resources to accommodate a rising population in coastal cities. However, coastal reclamation may impact the quality of the maritime ecosystem, including a decline in tide absorption and an increase in mild ocean pollution. A proper balance must be reached between the rate and size of ISA expansion and the demand for marine ecosystem services. In fact, dredging and regulation projects in the sea have produced impressive achievements over the past ten years.

While the total area of vegetation greatly decreases over the study period in the rapidly urbanizing area, the vegetation increases in some areas. This appears clearly in the northeast of Xiamen Island by comparing Figure 7. Our data reveal an impressively pronounced greening pattern in some areas of Xiamen City. The effect comes in large part from the ambitious park greening program and massive and intensive redevelopment of urban villages in Xiamen City. The findings support those of Zhang et al. [68], who found that the urbanized environment had both direct and indirect effects on vegetation growth, using 1 km-resolution data from 672 global cities.

The policy of redevelopment of urban villages was implemented in the 1980s when it was mainly occurring on Xiamen Island. The strategy aims to transform urban villages into high-rise residential areas while boosting green land cover. In the last ten years, the redevelopment of urban villages has appeared throughout Xiamen City due to rapid urbanization. Xiamen has more than 100 urban villages that have unique characteristics, with dense old low-rise buildings, low vegetation cover, crowded streets, and deep lanes. At present, some of them have been demolished and transformed into high-rise residential areas with high vegetation cover. Therefore, re-planning of urban villages and transforming them from urban villages to high-rise residential areas is an important approach to mitigate population and increase vegetation.

The policy to increase park greening aims to expand the green space of urban parks by building new parks or renewing the existing parks. Xiamen’s green space has been greatly expanded since 2016. Xiamen had 120 parks covering 26.04 km² in 2016, which rapidly increased to 342 parks with 83.68 km² of green space and 40.52 km² of green buffers by the end of 2020. The parks include various types, from large comprehensive urban parks to small community parks. Community parks are also called pocket parks and provide space for fitness, leisure, sightseeing, etc., which significantly improves the livability of the city and the happiness of its citizens.

5. Summary and Conclusions

In this study, we propose an FDTC algorithm to extract ISAs and the corresponding land cover from Landsat 5 TM, Landsat 8 OLI/TIRS, and Sentinel-2 images from 2009 to 2021 in Xiamen City, a coastal city in China. The performance of the FDTC was as-

sessed and compared with that of three other indices. Furthermore, we also explored the spatiotemporal variations in ISA and land cover in the study area.

The process of atmospheric correction is a crucial preprocessing step essential for numerous remote-sensing applications. In this study, a simplified DOS atmospheric correction model was first developed based on the original DOS model. However, the original DOS model invokes relatively complicated computations for atmospheric correction, so we developed a modified DOS to simplify the computation and facilitate application.

The aim of this study was to introduce a new FDTC method that can extract accurate ISA information from different medium- and high-resolution remotely sensed images by eliminating or reducing interference from wetlands, bare land, and vegetation. The results show that the FDTC approach performs better than other methods, such as BCI, PISI, and ABEL, for ISA extraction, achieving an average OA of 94.53%, KC of 0.855, and MICE of 0.851 between 2009 and 2021. In contrast, BCI, PISI, and ABEL produced lower average OA, KC, and MICE values. Additionally, using the proposed FDTC method for land cover mapping produced satisfactory results, with an average OA of 91.54%, KC of 0.877, and MICE of 0.877 from 2009 to 2021. The findings also suggest that the FDTC method compares well with other remote sensing indices and two open-source ISA products.

The FDTC method greatly improves the classification accuracy of ISA because the FDTC has some advantages. First, multispectral features (e.g., BCI, NDWI, MNDWI, BSI, WI, TB) were combined, and specialized knowledge was applied to avoid spectral confusion. The FDTC method adheres to a definite set of classification rules that remain consistent or undergo minor alterations. In addition, it separates ISA from bare land by using BCI and BSI or MFI, and it distinguishes wetlands from ISA and high-rise buildings by combining WI with TB.

The results show that ISA increased 0.60-fold over the past 13 years. The occupancy of vegetation, encroachment of bare land, and reclamation of coastal areas were the main causes of ISA's rapid expansion. The ISA increased most in the areas surrounding Haicang Bay, Malyuan Bay, Xinglin Bay, Tong'an Bay, Xiang'an new urban areas, and the second airport of Xiamen. Xiamen features a bay-like urban structure as a result of a past urban development strategy ("cross-island development") coupled with the coastline's natural restrictions on ISA expansion. Some areas in Xiamen became greener than they were 10 years ago. Our findings indicate a strikingly prominent greening pattern in some areas of Xiamen. The impact is primarily attributed to an ambitious park greening program and a massive and intensive redevelopment of urban villages in Xiamen City.

This study presents useful techniques for correcting atmospheric effects on remote images and mapping urban ISA and land cover, which facilitates the planning of sustainable urban structures. Nevertheless, this proposed method has some limitations. First, the parameters of the model cannot be calculated automatically. Thus, it is crucial to combine FDTC with the effective remote sensing image segmentation algorithm to obtain the parameters in a timely manner. Second, because FDTC uses a thermal infrared band to distinguish wetlands from high-rise buildings, some mixed pixels are generated when FDTC is applied to high-resolution Sentinel-2 images. In order to overcome this problem, the thermal infrared images must be refined by downscaling with land surface temperature. In addition, we utilized the DOS and sen2cor methods to eliminate the effects of the atmosphere on Landsat and Sentinel-2 images. However, to compare changes in FDTC parameters resulting from various atmospheric correction methods, future research should consider investigating other techniques, such as ACOLITE. Finally, this study uses FDTC only in one coastal city, so further experimentation should consider other areas with different environmental conditions using more medium- and high-resolution images.

Supplementary Materials: The following supporting information can be downloaded at: <https://www.mdpi.com/article/10.3390/su15107947/s1>, Figure S1. Comparisons of coefficient of variation (CV) for the raw images and their corrected products by atmospheric correction methods from 2009 to 2021.

Author Contributions: Conceptualization, software, investigation, and writing—original draft preparation, L.H.; methodology and funding acquisition, L.T.; data curation and references editing, H.W.; modification of the paper, H.Z. and L.L.; data collection, F.S. The published version of the manuscript has been read and approved by all authors. All authors have read and agreed to the published version of the manuscript.

Funding: This research was funded by the Fujian Natural Science Foundation (No. 2020J01265), the National Natural Science Foundation of China (No. 41471366).

Institutional Review Board Statement: Not applicable.

Informed Consent Statement: Not applicable.

Data Availability Statement: The data used in this work can be accessed by contacting the corresponding author.

Conflicts of Interest: The authors declare no conflict of interest.

Abbreviations

DTC	Decision tree classification
FDTC	Feature approach based on decision tree classification
ISAs	Impervious surface areas
NDWI	Normalized difference water index
MNDWI	Modified normalized difference water index
MFI	Mangrove forest index
BSI	Bare soil index
BCI	Biophysical composition index
GI	Greenness index
BI	Brightness index
WI	Wetness index
TB	Bright temperature
HSR	high-rise building shadows mixed with little roads
DN	Digital number
θ	Sun zenith angle
TOA	Top-of-the-atmosphere reflectance
DOS	Dark object subtraction
COST	A particular DOS approach calculating atmospheric transmittance using θ
$TAUv$	Atmospheric transmittance along the path from the earth's surface to the sensor
$TAUz$	Atmospheric transmittance along the path from the sun to the earth's surface
OA	Overall accuracy
KC	Overall kappa coefficient
MICE	Map-level image classification efficacy
A_{ISA}	Percent accuracy of ISA in common region between FDTC results and each ISA product
A_{NISA}	Percent accuracy of non-ISA in common region between FDTC results and each ISA product
GE	Google Earth
PISI	Perpendicular impervious surface index
ABEI	Automated built-up extraction index
NDISI	Normalized difference impervious surface index
NBAI	Normalized built-up area index
BAEI	Built-up Area Extraction index
BUI	Built-up index
EBBI	Enhanced built-up and bareness index
BLFEI	Built-up land features extraction index
OB-NNC	Object-based nearest neighbor classification
OSPs	Open-source ISA products
GAIA	Global artificial impervious area
DW	Dynamic world

References

1. Kuang, W.; Zhang, S.; Li, X.; Lu, D. A 30 m resolution dataset of China's urban impervious surface area and green space, 2000–2018. *Earth. Syst. Sci. Data* **2021**, *13*, 63–82. [[CrossRef](#)]
2. Zhao, S.; Liu, S.; Zhou, D. Prevalent vegetation growth enhancement in urban environment. *Proc. Natl. Acad. Sci. USA* **2016**, *113*, 6313–6318. [[CrossRef](#)] [[PubMed](#)]
3. Huang, F.; Yu, Y.; Feng, T. Automatic extraction of impervious surfaces from high resolution remote sensing images based on deep learning. *J. Vis. Commun. Image Represent.* **2019**, *58*, 453–461. [[CrossRef](#)]
4. Tian, Y.; Chen, H.; Song, Q.; Zheng, K. A novel index for impervious surface area mapping: Development and validation. *Remote Sens.* **2018**, *10*, 1521. [[CrossRef](#)]
5. Arnold, C.L., Jr.; Gibbons, C.J. Impervious surface coverage: The emergence of a key environmental indicator. *J. Am. Plann. Assoc.* **1996**, *62*, 243–258. [[CrossRef](#)]
6. Ranagalage, M.; Estoque, R.C.; Murayama, Y. An Urban Heat Island Study of the Colombo Metropolitan Area, Sri Lanka, Based on Landsat Data (1997–2017). *ISPRS Int. J. Geo-Inf.* **2017**, *6*, 189. [[CrossRef](#)]
7. Wang, M.; Xu, H. The impact of building height on urban thermal environment in summer: A case study of Chinese megacities. *PLoS ONE* **2021**, *16*, e0247786. [[CrossRef](#)]
8. Arifwidodo, S.; Chandrasiri, O.; Abdulharis, R.; Kubota, T. Exploring the effects of urban heat island: A case study of two cities in Thailand and Indonesia. *APN Sci. Bull.* **2019**, *9*, 539. [[CrossRef](#)]
9. Miller, J.D.; Hutchins, M. The impacts of urbanisation and climate change on urban flooding and urban water quality: A review of the evidence concerning the United Kingdom. *J. Hydrol. Reg. Stud.* **2017**, *12*, 345–362. [[CrossRef](#)]
10. Zeiger, S.J.; Hubbard, J.A. Urban stormwater temperature surges: A central US watershed study. *Hydrology* **2015**, *2*, 193–209. [[CrossRef](#)]
11. Santangelo, J.S.; Ness, R.W.; Cohan, B.; Fitzpatrick, C.R.; Innes, S.G.; Koch, S.; Lampei, C. Global urban environmental change drives adaptation in white clover. *Science* **2022**, *375*, 1275–1281. [[CrossRef](#)] [[PubMed](#)]
12. Weng, Q. Remote sensing of impervious surfaces in the urban areas: Requirements, methods, and trends. *Remote Sens. Environ.* **2012**, *117*, 34–49. [[CrossRef](#)]
13. Deng, H.; Liu, T.; Zhao, J. Strategic measures for an integrated approach to sustainable development in Lijiang City. *Int. J. Sust. Dev. World* **2011**, *18*, 559–562. [[CrossRef](#)]
14. Hua, L.; Zhang, X.; Nie, Q.; Sun, F.; Tang, L. The impacts of the expansion of urban impervious surfaces on urban heat islands in a coastal city in China. *Sustainability* **2020**, *12*, 475. [[CrossRef](#)]
15. Pal, M.; Mather, P.M. An assessment of the effectiveness of decision tree methods for land cover classification. *Remote Sens. Environ.* **2003**, *86*, 554–565. [[CrossRef](#)]
16. Xian, G.; Crane, M. An analysis of urban thermal characteristics and associated land cover in Tampa Bay and Las Vegas using Landsat satellite data. *Remote Sens. Environ.* **2006**, *104*, 147–156. [[CrossRef](#)]
17. Hu, B.; Xu, Y.; Huang, X.; Cheng, Q.; Ding, Q.; Bai, L.; Li, Y. Improving Urban Land Cover Classification with Combined Use of Sentinel-2 and Sentinel-1 Imagery. *ISPRS Int. J. Geo-Inf.* **2021**, *10*, 533. [[CrossRef](#)]
18. Voorde, T.V.D.; Roeck, T.D.; Canters, F. A comparison of two spectral mixture modelling approaches for impervious surface mapping in urban areas. *Int. J. Remote Sens.* **2009**, *30*, 4785–4806. [[CrossRef](#)]
19. Han, Y.; Liu, Y.; Hong, Z.; Zhang, Y.; Yang, S.; Wang, J. Sea ice image classification based on heterogeneous data fusion and deep learning. *Remote Sens.* **2021**, *13*, 592. [[CrossRef](#)]
20. Junaid, M.; Sun, J.; Iqbal, A.; Sohail, M.; Zafar, S.; Khan, A. Mapping LULC Dynamics and Its Potential Implication on Forest Cover in Malam Jabba Region with Landsat Time Series Imagery and Random Forest Classification. *Sustainability* **2023**, *15*, 1858. [[CrossRef](#)]
21. Li, J.; Song, C.; Cao, L.; Zhu, F.G.; Meng, X.L.; Wu, J.G. Impacts of landscape structure on surface urban heat islands: A case study of Shanghai, China. *Remote Sens. Environ.* **2011**, *115*, 3249–3263. [[CrossRef](#)]
22. Powell, R.L.; Roberts, D.A.; Dennison, P.E.; Hess, L.L. Sub-pixel mapping of urban land cover using multiple endmember spectral mixture analysis: Manaus, Brazil. *Remote Sens. Environ.* **2007**, *106*, 253–267. [[CrossRef](#)]
23. Zha, Y.; Gao, J.; Ni, S. Use of normalized difference built-up index in automatically mapping urban areas from TM imagery. *Int. J. Remote Sens.* **2003**, *24*, 583–594. [[CrossRef](#)]
24. Xu, H. A new index for delineating built-up land features in satellite imagery. *Int. J. Remote Sens.* **2008**, *29*, 4269–4276. [[CrossRef](#)]
25. Kawamura, M.; Jayamana, S.; Tsujiko, Y. Relation between social and environmental conditions in Colombo Sri Lanka and the urban index estimated by satellite remote sensing data. *Int. Soc. Photogramm. Remote Sens.* **1996**, *31*, 321–326.
26. Deng, C.; Wu, C. BCI: A biophysical composition index for remote sensing of urban environments. *Remote Sens. Environ.* **2012**, *127*, 247–259. [[CrossRef](#)]
27. Sun, G.; Chen, X.; Jia, X.; Yao, Y.; Wang, Z. Combinational built-up index (CBI) for effective impervious surface mapping in urban areas. *IEEE J. Sel. Top. Appl. Earth Obs. Remote Sens.* **2017**, *9*, 2081–2092. [[CrossRef](#)]
28. Firozjaei, M.K.; Sedighi, A.; Kiavarz, M.; Qureshi, S.; Haase, D.; Alavipanah, S.K. Automated built-up extraction index: A new technique for mapping surface built-up areas using Landsat 8 OLI imagery. *Remote Sens.* **2019**, *11*, 1966. [[CrossRef](#)]
29. Xu, H. Analysis of impervious surface and its impact on urban heat environment using the normalized difference impervious surface index (NDISI). *Photogramm. Eng. Remote Sens.* **2010**, *76*, 557–565. [[CrossRef](#)]

30. Waqar, M.M.; Mirza, J.F.; Mumtaz, R.; Hussain, E. Development of new indices for extraction of built-up area & bare soil from landsat data. *Open Access Sci. Rep.* **2012**, *1*, 136.
31. Bouzekri, S.; Lasbet, A.A.; Lachehab, A. A new spectral index for extraction of built-up area using landsat-8 data. *J. Indian Soc. Remote Sens.* **2015**, *43*, 867–873. [[CrossRef](#)]
32. As-Syakur, A.R.; Adnyana, I.W.S.; Arthana, I.W.; Nuarsa, I.W. Enhanced built-up and bareness index (EBBI) for mapping built-up and bare land in an urban area. *Remote Sens.* **2012**, *4*, 2957–2970. [[CrossRef](#)]
33. Kaimaris, D.; Patias, P. Identification and area measurement of the built-up area with the Built-up Index (BUI). *Int. J. Adv. Remote Sens. GIS* **2016**, *5*, 1844–1858. [[CrossRef](#)]
34. Bouhennache, R.; Bouden, T.; Taleb-Ahmed, A.; Cheddad, A. A new spectral index for the extraction of built-up land features from Landsat 8 satellite imagery. *Geocarto Int.* **2019**, *34*, 1531–1551. [[CrossRef](#)]
35. Lu, D.; Mausel, P. Assessment of atmospheric correction methods for Landsat TM data applicable to Amazon basin LBA research. *Int. J. Remote Sens.* **2002**, *23*, 2651–2671. [[CrossRef](#)]
36. Martins, V.S.; Barbosa, C.C.F.; De Carvalho, L.A.S.; Jorge, D.S.F.; Lobo, F.D.L.; Novo, E.M.L.D.M. Assessment of atmospheric correction methods for Sentinel-2 MSI images applied to Amazon floodplain lakes. *Remote Sens.* **2017**, *9*, 322. [[CrossRef](#)]
37. Kebede, T.A.; Hailu, B.T.; Suryabhagavan, K.V. Evaluation of spectral built-up indices for impervious surface extraction using Sentinel-2A MSI imagery: A case of Addis Ababa city, Ethiopia. *Environ. Chall.* **2022**, *8*, 100568. [[CrossRef](#)]
38. Deliry, S.I.; Avdan, Z.Y.; Avdan, U. Extracting urban impervious surfaces from Sentinel-2 and Landsat-8 satellite data for urban planning and environmental management. *Environ. Sci. Pollut. Res.* **2021**, *28*, 6572–6586. [[CrossRef](#)]
39. Tian, Y.; Yin, K.; Lu, D.; Hua, L.; Zhao, Q.; Wen, M. Examining land use and land cover spatiotemporal change and driving forces in Beijing from 1978 to 2010. *Remote Sens.* **2014**, *6*, 10593–10611. [[CrossRef](#)]
40. Tang, L.N.; Zhao, Y.; Yin, K.; Zhao, J. City profile: Xiamen. *Cities* **2013**, *31*, 615–624. [[CrossRef](#)]
41. Hua, L.Z.; Li, X.Q.; Tang, L.N.; Yin, K.; Zhao, Y. Spatio-temporal dynamic analysis of island-city landscape: A case study of Xiamen Island, China. *Int. J. Sust. Dev. World* **2010**, *17*, 273–278. [[CrossRef](#)]
42. Sola, I.; García-Martín, A.; Sandoñis-Pozo, L.; Álvarez-Mozos, J.; Pérez-Cabello, F.; González-Audícana, M.; Llovería, R.M. Assessment of atmospheric correction methods for Sentinel-2 images in Mediterranean landscapes. *Int. J. Appl. Earth. Obs.* **2018**, *73*, 63–76. [[CrossRef](#)]
43. Chander, G.; Markham, B.L.; Helder, D.L. Summary of current radiometric calibration coefficients for Landsat MSS, TM, ETM+, and EO-1 ALI sensors. *Remote Sens. Environ.* **2009**, *113*, 893–903. [[CrossRef](#)]
44. Chavez, P.S. Image-based atmospheric corrections-revisited and improved. *Photogramm. Eng. Remote Sens.* **1996**, *62*, 1025–1036.
45. Ramsey, R.D.; Wright, D.L.; McGinty, C. Evaluating the use of Landsat 30m enhanced thematic mapper to monitor vegetation cover in shrub-steppe environments. *Geocarto Int.* **2004**, *19*, 39–47. [[CrossRef](#)]
46. Xu, H. Retrieval of the reflectance and land surface temperature of the newly-launched Landsat 8 satellite. *Chin. J. Geophys.* **2015**, *58*, 741–747. (In Chinese)
47. Yang, X.; Lo, C.P. Relative radiometric normalization performance for change detection from multi-date satellite images. *Photogramm. Eng. Remote Sens.* **2000**, *66*, 967–980.
48. Friedl, M.A.; Brodley, C.E. Decision tree classification of land cover from remotely sensed data. *Remote Sens. Environ.* **1997**, *61*, 399–409. [[CrossRef](#)]
49. Punia, M.; Joshi, P.K.; Porwal, M.C. Decision tree classification of land use land cover for Delhi, India using IRS-P6 AWiFS data. *Expert Syst. Appl.* **2011**, *38*, 5577–5583. [[CrossRef](#)]
50. Qi, Z.; Yeh, A.G.O.; Li, X.; Lin, Z. A novel algorithm for land use and land cover classification using RADARSAT-2 polarimetric SAR data. *Remote Sens. Environ.* **2012**, *118*, 21–39. [[CrossRef](#)]
51. McFeeters, S.K. The use of the Normalized Difference Water Index (NDWI) in the delineation of open water features. *Int. J. Remote Sens.* **1996**, *17*, 1425–1432. [[CrossRef](#)]
52. Xu, H. Modification of normalised difference water index (NDWI) to enhance open water features in remotely sensed imagery. *Int. J. Remote Sens.* **2006**, *27*, 3025–3033. [[CrossRef](#)]
53. Xu, H.; Wang, M.; Shi, T.; Guan, H.; Fang, C.; Lin, Z. Prediction of ecological effects of potential population and impervious surface increases using a remote sensing based ecological index (RSEI). *Ecol. Indic.* **2018**, *93*, 730–740. [[CrossRef](#)]
54. Rikimaru, A.; Roy, P.S.; Miyatake, S. Tropical Forest cover density mapping. *Trop. Ecol.* **2002**, *43*, 39–47.
55. Jia, M.; Wang, Z.; Wang, C.; Mao, D.; Zhang, Y. A new vegetation index to detect periodically submerged mangrove forest using single-tide sentinel-2 imagery. *Remote Sens.* **2019**, *11*, 2043. [[CrossRef](#)]
56. Crist, E.P. A TM tasseled cap equivalent transformation for reflectance factor data. *Remote Sens. Environ.* **1985**, *17*, 301–306. [[CrossRef](#)]
57. Baig, M.H.; Zhang, L.; Shuai, T.; Tong, Q. Derivation of a tasseled cap transformation based on Landsat 8 at-satellite reflectance. *Remote Sens. Lett.* **2014**, *5*, 423–431. [[CrossRef](#)]
58. Shi, T.; Xu, H. Derivation of Tasseled Cap Transformation coefficients for Sentinel-2 MSI at-sensor reflectance data. *IEEE J.-Stars.* **2019**, *12*, 4038–4048. [[CrossRef](#)]
59. Li, F.; Jackson, T.J.; Kustas, W.P.; Schmugge, T.J.; French, A.N.; Cosh, M.H.; Bindlish, R. Deriving land surface temperature from Landsat 5 and 7 during SMEX02/SMACEX. *Remote Sens. Environ.* **2004**, *92*, 521–534. [[CrossRef](#)]

60. Congalton, R.G. A review of assessing the accuracy of classifications of remotely sensed data. *Remote Sens. Environ.* **1991**, *37*, 35–46. [[CrossRef](#)]
61. Landis, J.R.; Koch, G.G. The measurement of observer agreement for categorical data. *Biometrics* **1977**, *33*, 159–174. [[CrossRef](#)]
62. Shao, G.; Tang, L.; Liao, J. Overselling overall map accuracy misinforms about research reliability. *Landsc. Ecol.* **2019**, *34*, 2487–2492. [[CrossRef](#)]
63. Shao, G.; Tang, L.; Zhang, H. Introducing image classification efficacies. *IEEE Access* **2021**, *9*, 134809–134816. [[CrossRef](#)]
64. Gong, P.; Li, X.; Wang, J.; Bai, Y.; Chen, B.; Hu, T.; Zhou, Y. Annual maps of global artificial impervious area (GAIA) between 1985 and 2018. *Remote Sens. Environ.* **2020**, *236*, 111510. [[CrossRef](#)]
65. Brown, C.F.; Brumby, S.P.; Guzder-Williams, B.; Birch, T.; Hyde, S.B.; Mazzariello, J.; Tait, A.M. Dynamic World, Near real-time global 10 m land use land cover mapping. *Sci. Data* **2022**, *9*, 251. [[CrossRef](#)]
66. Chen, Y.; Zhang, G.; Cui, H.; Li, X.; Hou, S.; Ma, J.; Li, Z.; Li, H.; Wang, H. A novel weakly supervised semantic segmentation framework to improve the resolution of land cover product. *ISPRS Photogramm. Eng. Remote Sens.* **2023**, *196*, 73–92. [[CrossRef](#)]
67. Lin, T.; Xue, X.; Shi, L.; Gao, L. Urban spatial expansion and its impacts on island ecosystem services and landscape pattern: A case study of the island city of Xiamen, Southeast China. *Ocean Coast. Manag.* **2013**, *81*, 90–96. [[CrossRef](#)]
68. Zhang, L.; Yang, L.; Zohner, C.M.; Crowther, T.W.; Li, M.; Shen, F.; Zhou, C. Direct and indirect impacts of urbanization on vegetation growth across the world's cities. *Sci. Adv.* **2022**, *8*, eabo0095. [[CrossRef](#)] [[PubMed](#)]

Disclaimer/Publisher's Note: The statements, opinions and data contained in all publications are solely those of the individual author(s) and contributor(s) and not of MDPI and/or the editor(s). MDPI and/or the editor(s) disclaim responsibility for any injury to people or property resulting from any ideas, methods, instructions or products referred to in the content.